

POLITECNICO DI TORINO

Master's Degree in Mechanical Engineering



Master's Degree Thesis

Structural analysis of a Cirrus SR22 wing box through classical FEM and CUF

Supervisors

Prof. Matteo Filippi

Prof. Marco Petrolo

Prof. Dario Magliacano

Candidate

Deepak Nelmangala Chandrashekhar

October 2024

Summary

This thesis explores the structural analysis of the central wing box of the Cirrus SR22 aircraft using both the Carrera Unified Formulation (CUF) and Abaqus software. The Cirrus SR22 is a widely respected single-engine aircraft, known for its composite construction and the integration of critical components such as the central wing box, which plays a pivotal role in the aircraft's structural integrity. The central wing box is essential for connecting the wings to the fuselage and supports the forces generated during flight, making it a critical focus for analysis.

The study begins by introducing the Cirrus SR22, detailing its design and the importance of the central wing box. It then discusses the materials used in the wing box, including isotropic and composite materials, which are evaluated for their performance under various conditions. The thesis emphasizes the significance of material selection in aerospace applications, where the balance between weight, strength, and durability is crucial for optimizing aircraft performance.

The core of the thesis is dedicated to the application of CUF, a powerful and versatile approach within the Finite Element Method (FEM). CUF is highlighted for its ability to handle complex geometries and material behaviours, particularly in the context of advanced aerospace materials like composites. The study contrasts CUF with traditional FEM methods, showing how CUF's use of higher-order polynomial expansions leads to more accurate and computationally efficient analyses, particularly for structures like the central wing box.

Failure analysis is also a key component of the thesis, where different failure criteria, such as the Tsai-Wu and Maximum Stress Criteria, are applied to predict the onset of failure in composite materials. The integration of failure indices into the analysis enhances the understanding of potential weak points in the structure, which is critical for ensuring the safety and reliability of the aircraft.

Overall, this thesis provides a comprehensive analysis of the central wing box, demonstrating the effectiveness of CUF and Abaqus in evaluating the structural integrity and failure potential of this critical component. The findings contribute valuable insights into the design and optimization of aerospace structures, with implications for improving the performance and safety of modern aircraft.

Acknowledgements

I would like to express my deepest gratitude to God, whose grace and guidance have sustained me throughout this journey and to all those who have supported me throughout this journey, which has culminated in the completion of this thesis. First and foremost, I am profoundly thankful to my supervisor, **Professor Matteo Filippi**, whose guidance and support have been invaluable. His expert advice and encouragement provided me with the confidence to pursue and refine my research ideas. I am grateful for the countless hours he spent reviewing my work and for his dedication to my academic and professional development.

I also extend my sincere thanks to my co-supervisors, **Professor Dario Magliacano** and **Professor Marco Petrolo**. Professor Magliacano, in particular, has played a pivotal role in my research. His insightful feedback and unwavering dedication to my progress laid a solid foundation for this thesis. He was always available to offer his expertise, whether through detailed discussions or quick clarifications. His ability to challenge my thinking while offering constructive advice significantly shaped my academic growth. I am profoundly grateful for his mentorship, which has been instrumental not only in the completion of this thesis but also in my development as a professional. Thank you, **Professor Dario Magliacano**, for believing in me and for being a constant source of inspiration.

To **Professor Marco Petrolo**, I am also deeply thankful. His support and insights contributed greatly to the direction and refinement of my work. His ability to offer a fresh perspective and his readiness to engage with my research helped me overcome numerous challenges along the way.

In addition to my academic mentors, I would like to extend my heartfelt thanks to my family, my friends Micah and Presley. Their unwavering support, encouragement, and patience provided me with the strength to keep pushing forward, even during the most challenging times. I am especially grateful to my parents, whose love and belief in me have been a constant source of motivation. Finally, to everyone who believed in me and supported me in various ways, thank you. Your contributions, no matter how small, made a meaningful impact on this journey, and I will always be grateful for your presence in my life.

Table of Contents

List of Tables	VII
List of Figures	VIII
Acronyms	XII
1 Introduction	1
1.1 Cirrus SR22 Aircraft	1
1.2 Central Wing Box	2
1.3 Materials and Model used in thesis	3
1.4 Overview of CUF	6
1.5 Overview of failure index	8
2 Carrera Unified Formulation and Failure analysis	10
2.1 Governing equations in matrix form	10
2.1.1 Geometrical relations	10
2.1.2 Constitutive equation	13
2.2 Carrera Unified Formulation approach	15
2.2.1 Beam 1D CUF-FEM Finite Element	16
2.2.2 Plate 2D CUF-FEM Finite Element	17
2.2.3 Taylor Expansion Model	18
2.2.4 Lagrange Expansion Model	19
2.3 Failure Analysis	21
2.3.1 Failure criteria	21
2.3.2 Maximum Stress Criterion	21
2.3.3 Tsai-Wu Criterion	22
2.3.4 Tsai-Hill Criterion	23
3 Analysis	25
3.1 Analysis Using Abaqus	25
3.2 Analysis Using CUF	29

3.3	Modal analysis of Central Wing Box	37
3.3.1	Analysis overview	37
3.3.2	Conclusion	43
3.4	Static Analysis of Central Wing Box	44
3.4.1	Analysis Overview	44
3.4.2	Conclusion	60
3.5	Failure Analysis For The Composite Materials	61
3.5.1	Analysis Overview	61
3.5.2	Conclusion	68
4	Conclusion and Future Perspectives	73
	Bibliography	76

List of Tables

3.1	Frequency Table.	38
3.2	Properties and Densities of the materials used.	62
3.3	Mechanical properties of materials: Young's Modulus.	62
3.7	Stacking Sequence, von Mises stress, and Deformation for Std CF Fabric.	62
3.4	Mechanical properties of materials: Shear Modulus.	63
3.5	Mechanical properties of materials: Poisson's Ratio.	63
3.8	Stacking Sequence, von Mises stress, and Deformation for E glass Fabric	63
3.6	Ultimate Strength of Materials.	64
3.9	Stacking Sequence, von Mises stress, and Deformation for Std CF UD.	64
3.10	Stacking Sequence, von Mises stress, and Deformation for M55 UD.	64
3.11	Stacking Sequence, von Mises stress, and Deformation for E glass UD.	65
3.12	Stacking Sequence, von Mises stress, and Deformation for Kevlar UD.	65
3.13	Stacking Sequence, von Mises stress, and Deformation for Boron UD.	65
3.14	Failure Index values for Std CF Fabric.	66
3.15	Failure Index values for E glass Fabric.	66
3.16	Failure Index values for Std CF UD.	66
3.17	Failure Index values for M55 UD.	66
3.18	Failure Index values for E glass UD.	67
3.19	Failure Index values for Kevlar UD.	67
3.20	Failure Index values for Boron UD.	67

List of Figures

1.1	Cirrus SR22-G6 turbo 2023 model [2].	1
1.2	Central wing box [6].	3
1.3	Aircraft components that incorporate composite materials [11].	5
1.4	Failure Phenomena[15]	8
2.1	Geometry and adopted reference system [19].	11
2.2	Fiber Orientation angle [19].	14
2.3	Beam structure.	16
2.4	Plate 2D model.	18
2.5	Cross section L-elements in natural geometry.	19
2.6	Lagrange Q4 linear phase element: from material to natural ref.frame.	20
3.1	Boundary Condition.	26
3.2	Load Condition 1.	26
3.3	Load Condition 2.	27
3.4	Load Condition 3.	27
3.5	Load Condition 4.	28
3.6	Load Condition 5.	28
3.7	Gravity.	29
3.8	Input Folder	30
3.9	Structural Model Requirements	31
3.10	Boundary Condition.DAT file with D-point.	32
3.11	Boundary Condition.DAT file with F-point.	32
3.12	Nodes.DAT file	33
3.13	Connectivity.DAT file	34
3.14	Exp_mesh.DAT file.	34
3.15	Exp_CONN.DAT file.	35
3.16	ISO-M Material.DAT file.	35
3.17	Ort-M.DAT file.	36
3.18	MUL2	36
3.19	Mode Shape 1.	39

3.20	Mode Shape 2.	39
3.21	Mode Shape 3.	40
3.22	Mode Shape 4.	40
3.23	Mode Shape 5.	41
3.24	Mode Shape 6.	41
3.25	Mode Shape 7.	42
3.26	Mode Shape 8.	42
3.27	Mode Shape 9.	43
3.28	Mode Shape 10.	43
3.29	Aluminium solid deformation Using Classical FEM.	46
3.30	Aluminium shell deformation using Classical FEM.	46
3.31	Aluminium deformation Using CUF.	47
3.32	STD CF Fabric solid deformation using Classical FEM.	47
3.33	STD CF Fabric Shell deformation using Classical FEM.	48
3.34	STD CF Fabric deformation using CUF.	48
3.35	E Glass Fabric solid deformation using Classical FEM.	49
3.36	E Glass Fabric Shell deformation using Classical FEM.	49
3.37	E Glass Fabric deformation using CUF.	50
3.38	Kevlar Fabric solid deformation using Classical FEM.	50
3.39	Kevlar Fabric shel deformation using Classical FEM.	51
3.40	Kevlar Fabric deformation using CUF.	51
3.41	STD CF UD solid deformation using Classical FEM.	52
3.42	STD CF UD shell deformation using Classical FEM.	52
3.43	STD CF UD deformation using CUF.	53
3.44	HMCF UD solid deformation using Classical FEM.	53
3.45	HMCF UD Shell deformation using Classical FEM.	54
3.46	HMCF UD deformation using CUF.	54
3.47	M55 UD solid deformation using Classical FEM	55
3.48	M55 UD shell deformation using Classical FEM.	55
3.49	M55 UD deformation using CUF.	56
3.50	E Glass UD solid deformation using Classical FEM.	56
3.51	E Glass UD Shell deformation using Classical FEM.	57
3.52	E Glass UD deformation using CUF.	57
3.53	Kevlar UD solid deformation using Classical FEM.	58
3.54	Kevlar UD Shell deformation using Classical FEM.	58
3.55	Kevlar UD Deformation Using CFU.	59
3.56	Boron UD solid deformation using Classical FEM.	59
3.57	Boron UD Shell deformation using Classical FEM.	60
3.58	Boron UD deformation using CUF	60
3.59	Failure index chart with respect to material and stacking sequence.	68
3.60	E Glass Fabric 45°/ - 45°/0°/90°.	69

3.61 E Glass Fabric $45^\circ / -45^\circ / 45^\circ / -4^\circ$	70
3.62 E Glass Fabric $60^\circ / 30^\circ / -30^\circ / -60^\circ$	70
3.63 E Glass UD $45^\circ / -45^\circ / 0^\circ / 90^\circ$	71
3.64 E Glass UD $45^\circ / -45^\circ / 45^\circ / -45^\circ$	71
3.65 E Glass UD $60^\circ / 30^\circ / -30^\circ / -60^\circ$	72

Acronyms

CUF

Carrera Unified Formulation

FEM

Finite Element Method

Std

Standard

CF

Carbon Fiber

UD

Unidirectional

HMCF

High Modulus Carbon Fiber

M55

Specific grade of High Modulus Carbon Fiber

SR

Single Reciprocating

GA

General Aviation

CAPS

Cirrus Airframe Parachute System

Chapter 1

Introduction

1.1 Cirrus SR22 Aircraft

Cirrus Aircraft, based in Duluth, Minnesota, has been manufacturing the Cirrus SR22, a composite single-engine aircraft with seating for four to five passengers, since 2001. The SR22 is an enhanced version of the Cirrus SR20, featuring a larger wing, increased fuel capacity, and a more powerful engine rated at 310 horsepower (231 kW), or 315 horsepower (235 kW) for the turbocharged model. It also pioneered the use of a full glass cockpit in light aircraft within the general aviation (GA) sector. [1].



Figure 1.1: Cirrus SR22-G6 turbo 2023 model [2].

The SR22, which received certification in November 2000, serves as a more

robust version of its predecessor, the SR20. Production began in 2001. The SR22 is a low-wing cantilever monoplane constructed from composite materials, featuring fixed tricycle landing gear, a castering nose wheel, and differential braking on the main wheels for steering control. Its engine, a Continental IO-550-N with 310 horsepower (231 kilowatts), is mounted at the aircraft's front. The cabin, which seats four, is accessible through doors on both sides of the fuselage. [3]. Similar to the SR20, the Cirrus SR22 is equipped with the Cirrus Airframe Parachute System (CAPS), which allows the entire aircraft to descend safely to the ground in emergencies.[4]. The Cirrus SR22 is widely regarded as a high-performance aircraft with several critical components. Key elements of the SR22 include the fuselage, wings, empennage (tail section), engine, propeller, landing gear, avionics (instrumentation and control systems), control surfaces (ailerons, elevators, rudder), fuel system, and electrical system. This study focuses on the central wing box, an important structural component of the wing, evaluating various materials using different analytical methods.

1.2 Central Wing Box

In aviation, the center wing box is a crucial structure that connects the main wings to the fuselage. It also integrates parts such as the main landing gear doors and the wing-to-body fairing. A schematic representation of the wing and wing box is shown in the Figure 1.2. The wings are attached to the center wing box, which is housed within the fuselage structure. Under bending loads, the maximum stress is concentrated on the wing box.

The primary role of the central wing box goes beyond just structural support, as it distributes the significant forces generated during flight. This compact yet critical component not only securely fastens the wings but also accommodates vital systems like fuel storage, hydraulic lines, and electrical wiring. Such an intricate design optimizes space, which is essential for maintaining the aircraft's balance and efficiency. [5]. Additionally, the central wing box showcases a fine balance in engineering, emphasizing both structural durability and weight efficiency. The design prioritizes reducing weight without sacrificing strength, which contributes to fuel efficiency and environmental performance improvements. This weight reduction approach also decreases drag, thereby improving aerodynamic performance through its smooth integration with the wing structure. As a result, the central wing box stands as a hallmark of modern aerospace engineering, combining functional necessity with technological advancements in aircraft design. [5].

The wing box consists of two major components. The internal wing structure is made up of spars and ribs, while the external wing structure is the skin. Wing Skin: In many aircraft, the wing skin performs multiple roles. It provides the aerodynamic

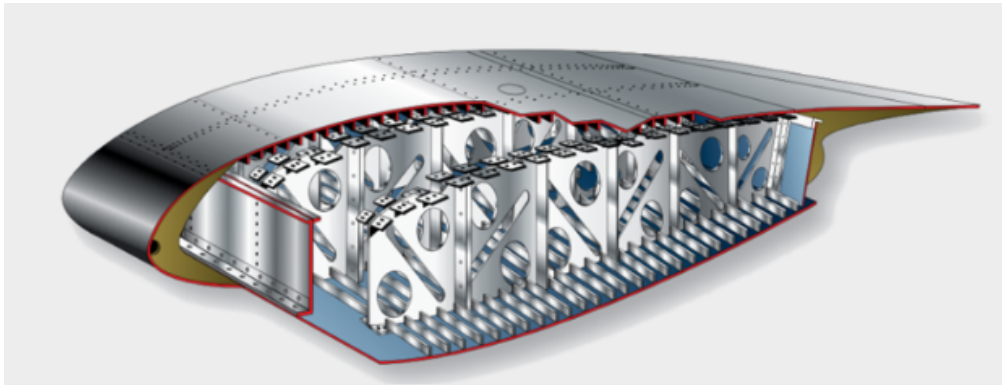


Figure 1.2: Central wing box [6].

shape, carries part of the structural loads, supports torsional loads, serves as fuel tanks, and facilitates inspection and maintenance. **Ribs:** In an aircraft, ribs form key structural elements within the wing. Typically, ribs help maintain the aerofoil shape of the wing, with the skin adopting this form when stretched over the ribs. These ribs are essential for supporting wing panels, ensuring and preserving the aerodynamic shape, transmitting large forces, adding strength, preventing buckling, and separating individual fuel tanks within the wing. **Spar:** In fixed-wing aircraft, the spar is the main structural member of the wing, running lengthwise, usually perpendicular to the fuselage (or at an angle depending on wing sweep). The spar bears the loads experienced during flight and supports the weight of the wings while on the ground, primarily handling shear forces and bending moments.[7].

Moreover, the spar functions as the backbone of the wing, enduring flight loads and supporting wing weight during both flight and ground operations. This critical function highlights its role in maintaining the structural integrity of the central wing box, where the integration of spars, ribs, and skin creates a sturdy framework capable of withstanding considerable aerodynamic forces and operational stress. This section will detail the way each component, including the spar, contributes to the strength of the central wing box, ensuring the aircraft remains safe and functional across varying conditions. The upcoming sections will investigate how different materials influence the structural integrity of the central wing box.

1.3 Materials and Model used in thesis

Finite Element Analysis (FEA) is a vital computational method commonly used in engineering and applied sciences to predict how structures and materials behave under various physical conditions. This technique breaks down a complex structure into smaller, manageable finite elements, which are then analyzed both individually

and collectively to understand the system's overall response. A crucial aspect of FEA is selecting the appropriate element types, as this choice significantly affects the accuracy and efficiency of the analysis. Different types of elements, such as 1D, 2D, and 3D, are suited for specific applications and geometries, allowing for detailed modeling of diverse structural challenges. Careful selection of the right element type ensures the model accurately captures necessary physical behaviors while optimizing computational resources. In this regard, understanding the characteristics and uses of various elements, especially solid and shell types, is essential. This section will explore these two fundamental element types, emphasizing their significance, applications, and considerations for different structural analyses [8].

Solid models offer detailed representations through the use of three-dimensional elements. These models are especially useful for capturing complex stress states, including stress distribution through the thickness of a material. For example, solid models can accurately predict the behavior of adhesive bonds and delamination in composite materials, often found in wind turbine blades. However, these models require significant computational resources due to the high number of elements and the complexity of the simulations. Solid models are ideal for instances where detailed local stress analysis is required, particularly under torsional loads or when evaluating damage progression.

Shell models, in contrast, use two-dimensional elements to represent a three-dimensional structure. These models are less complex and more computationally efficient compared to solid models. They are commonly used to analyze the global structural behavior of blades, specifically for assessing overall displacement and longitudinal strain. Shell models are typically sufficient for many types of analysis, particularly those involving bending loads, and are often used in the early stages of design due to their computational efficiency.

In summary, while both solid and shell models can yield similar overall results, solid models provide more detailed local insights at a higher computational cost, whereas shell models strike a balance between accuracy and efficiency, making them well-suited for global structural analysis [9]. Selecting the appropriate material for a component based on its application is essential due to various critical factors, such as performance, durability, weight, cost, and the specific environmental and operational conditions. This decision directly impacts the component's efficiency, safety, and lifespan, which is particularly important in industries like aerospace, automotive, and civil engineering. In aviation, for instance, the choice of material affects an aircraft's weight, fuel efficiency, structural integrity, and resistance to harsh operational conditions. Materials like isotropic, orthotropic, and composite materials have distinct properties that make them suitable for specific purposes. Isotropic materials, such as aluminum and titanium, exhibit uniform properties in all directions and are valued for their reliability and predictability, making them common in many aircraft structural components. Aluminum, prized for its excellent

strength-to-weight ratio and corrosion resistance, is extensively used in airframes, while titanium, though more costly, offers superior strength and heat resistance, making it ideal for high-performance parts like jet engine components. Orthotropic materials, found in many composites, have different properties along three mutually perpendicular axes. These materials are designed to provide maximum strength and stiffness where it's needed most while minimizing weight. In aerospace, carbon fiber-reinforced polymers (CFRPs) are a prime example of orthotropic materials, widely used in modern aircraft due to their excellent strength-to-weight ratio, fatigue resistance, and adaptability to specific structural needs. CFRPs play a crucial role in primary structures like wings and fuselages, seen in aircraft like the Boeing 787 and Airbus A350. Their use in these areas demonstrates their importance in achieving advanced aerodynamic performance and fuel efficiency. The advancement of computational structures technology and composite materials over the past 30 years has led to improvements in structural performance, reduced operational risk, and faster development times. Design challenges for new systems include cost-effectiveness, safety, and environmental sustainability. For military aircraft, emphasis is shifting from maximum performance to acceptable performance at a lower cost. In space exploration, the focus is moving from long-term, complex missions to simpler, more cost-effective, and faster missions. For future aeronautical and space systems, materials and structural innovations will remain crucial to determining reliability, performance, and cost-efficiency. In some future aircraft, advancements in structural technologies may significantly lower operating costs and reduce overall weight more than other technological improvements[10].



Figure 1.3: Aircraft components that incorporate composite materials [11].

The use of composite materials provides significant advantages, as these materials often have superior specific properties compared to traditional metals. For example,

a composite structure can have up to ten times the stiffness and half the density of an aluminum structure. This is why "full composite" designs are common in advanced vehicles. Designers are constantly looking for lighter, stronger materials to improve performance, with reducing material density being one of the most effective ways to reduce weight and enhance efficiency. Understanding the behaviour and appropriate application of these materials is not only fundamental for structural integrity but also for optimizing the overall performance and efficiency of the components. The below table shows all the materials used and their material properties.

Material ID	Material	Density rho [kg/m ³]
1	Std CF Fabric	1600
2	E glass Fabric	1900
3	Kevlar Fabric	1400
4	Std CF UD	1600
5	HMCF UD	1600
6	M55 UD	1650
7	E glass UD	1900
8	Kevlar UD	1400
9	Boron UD	2000

Material ID	Young's Modulus (Pa)			Shear Modulus(Pa)			Poisson's Ratio		
	E1	E2	E3	G12	G13	G23	NU12	NU13	NU23
1	7.00E+11	7.00E+11	5.19E+10	5.00E+10	2.29E+10	2.29E+10	0.1	0.13	0.13
2	2.50E+11	2.50E+11	5.00E+10	4.00E+10	1.98E+10	1.98E+10	0.2	0.26	0.26
3	3.00E+11	3.00E+11	2.40E+10	5.00E+10	9.52E+09	9.52E+09	0.2	0.26	0.26
4	1.35E+12	8.00E+11	1.00E+11	5.00E+10	5.00E+10	3.60E+10	0.3	0.3	0.39
5	1.75E+12	8.00E+10	8.00E+10	5.00E+10	5.00E+10	2.88E+10	0.3	0.3	0.39
6	3.00E+11	1.20E+11	1.20E+11	5.00E+10	5.00E+10	4.32E+10	0.3	0.3	0.3
7	4.00E+11	8.00E+10	8.00E+10	4.00E+10	4.00E+10	3.02E+10	0.25	0.25	0.325
8	7.50E+11	6.00E+11	6.00E+10	2.00E+10	2.00E+10	2.08E+10	0.34	0.34	0.442
9	2.00E+12	1.50E+11	1.50E+11	5.00E+10	5.00E+10	5.77E+10	0.23	0.23	0.299

1.4 Overview of CUF

The Carrera Unified Formulation (CUF) is a versatile and powerful approach within the finite element method (FEM) framework designed to handle a wide range of structural analysis problems [12]. Developed by Erasmo Carrera and detailed in the provided document, CUF offers a unified methodology for formulating finite element models that can efficiently handle complex geometries and material behaviours,

including isotropic, orthotropic, and composite materials. The core advantage of CUF lies in its ability to generalize the governing equations of structural mechanics in a consistent manner across different structural theories, such as beam, plate, and shell models. This flexibility allows CUF to seamlessly transition between different structural theories within the same framework, ensuring consistency and reducing potential errors in the modelling process, particularly for aerospace structures that often involve intricate assemblies of various components and materials.

One of the primary reasons for the increased accuracy of CUF compared to traditional FEM methods is its ability to employ higher-order polynomial expansions in the displacement field representation [13]. Traditional FEM methods typically rely on linear or low-order polynomial approximations, which can limit their ability to capture complex variations in displacement, stress, and strain within the elements. CUF, on the other hand, can utilize higher-order terms to more precisely model these variations, leading to a more accurate representation of the structural behaviour. This is especially important in regions with high stress gradients or complex geometries, where traditional methods might fall short. Additionally, CUF's capability to accurately represent the anisotropic properties of advanced composite materials, such as orthotropic materials, enhances its precision. This accurate representation is achieved through refined kinematic models that can capture detailed local phenomena, such as interlaminar stresses and deformation patterns, which are critical for reliable design and analysis in aerospace engineering.

Furthermore, CUF enhances the computational efficiency of finite element analyses by enabling higher-order approximations and reducing the number of elements required to achieve accurate results. This computational efficiency is particularly beneficial when dealing with large-scale problems, such as the analysis of entire aircraft structures, where computational resources and time are significant considerations. The ability to incorporate various kinematic models and degrees of freedom within the same framework allows CUF to capture detailed local phenomena crucial for aerospace components. By allowing for finer meshes and more detailed analyses within practical timeframes, CUF makes it feasible to conduct comprehensive and precise analyses that might be computationally prohibitive with traditional FEM methods. This combination of higher accuracy and computational efficiency makes CUF an indispensable tool for modern structural analysis, particularly in complex and demanding fields like aerospace engineering [14].

In summary, the Carrera Unified Formulation (CUF) represents a significant advancement in finite element analysis, offering a robust, adaptable, and efficient method for analysing a wide range of structural problems. CUF's application to the analysis of the central wing box in this thesis highlights its capability to handle both isotropic materials like aluminium and complex orthotropic materials. This unified approach integrates various structural theories—such as beam, plate, and shell models—within a single framework, ensuring consistency and reducing potential

errors. The use of higher-order polynomial expansions in the displacement field representation allows CUF to more accurately capture variations in displacement, stress, and strain, particularly in regions with high stress gradients or complex geometries. Furthermore, CUF's precise modelling of advanced material behaviours, including the accurate representation of anisotropic properties in composite materials, enhances the reliability of the analysis. The computational efficiency of CUF, achieved through higher-order approximations and reduced element requirements, enables detailed and comprehensive analyses of large-scale structures, making it particularly suitable for complex structural analyses in aerospace engineering where accurate predictions of structural performance and behaviour are critical.

1.5 Overview of failure index

Composite materials are increasingly being used in many engineering fields since their excellent specific properties are advantageous for the design of many structures, such as aircraft or cars. The characterization of failure mechanisms is a crucial issue to fully exploit composite material capabilities. As shown in Figure 1.4, various phenomena as matrix micro cracking, delamination between plies, debonding between fibre and matrix material (pull-out) can lead to the failure of composite structures. A failure index is a crucial numerical value used in the analysis and

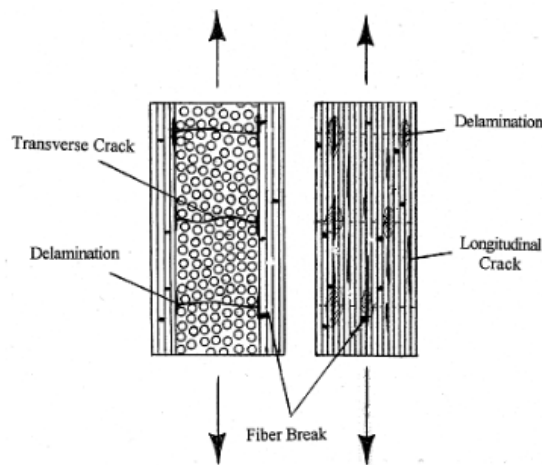


Figure 1.4: Failure Phenomena[15]

design of composite materials to predict the onset and location of failure under specific loading conditions. This predictive capability ensures the safety and reliability of structures made from composites by identifying potential weak points and enabling their reinforcement. Unlike traditional strength analysis methods,

which are often designed for homogeneous and isotropic materials, failure indices are tailored for the anisotropic and heterogeneous nature of composites. This allows for a more accurate prediction of failure under complex, multi-axial stress states typical in composite applications. Furthermore, failure indices offer a more efficient alternative to empirical testing, reducing costs and time associated with extensive physical tests. They provide detailed insights into different failure modes, enhancing the design optimization process and material efficiency. In advanced applications such as aerospace and automotive industries, failure indices are integrated into Finite Element Analysis (FEA) software, offering a comprehensive approach to understanding local failure mechanisms and enabling the development of high-performance, lightweight structures. Thus, the failure index not only ensures the structural integrity and longevity of composite materials but also facilitates their innovative use in various high-stakes applications.

Chapter 2

Carrera Unified Formulation and Failure analysis

This chapter is devoted to the description of the Finite Element Method and Carrera Unified Formulation. For decades, many efforts have been dedicated to the derivation of advanced theories able to tackle various structural problems. To solve some of the issues related to classical approaches, CUF was introduced as a generator of structural theories for beams, plates and shells [16].

The Carrera Unified Formulation (CUF) is a generalised hierarchical framework to derive higher-order 1D (beam) and 2D (plate, shell) structural theories. The fundamental concept of the framework is the introduction of expansion functions, in addition to standard finite element interpolation functions, to enrich the kinematic description of the beam cross-section and plate/shell thickness. This approach leads to 1D and 2D CUF models which are similar to 3D-FEA in terms of solution accuracy, but require considerably less computational effort [17] [18].

2.1 Governing equations in matrix form

2.1.1 Geometrical relations

The adopted rectangular cartesian coordinate system is shown in Figure 2.1, together with the geometry of a beam structure. The cross-section of the beam lies on the xz -plane and it is denoted by Ω , whereas the boundaries over y are $0 \leq y \leq L$.

Let \mathbf{u} be the continuous displacement field of the body, the function of the material point expressed as column vector:

$$\mathbf{u} = \mathbf{u}(x, y, z) = \{u(x, y, z), v(x, y, z), w(x, y, z)\}^T \quad (2.1)$$

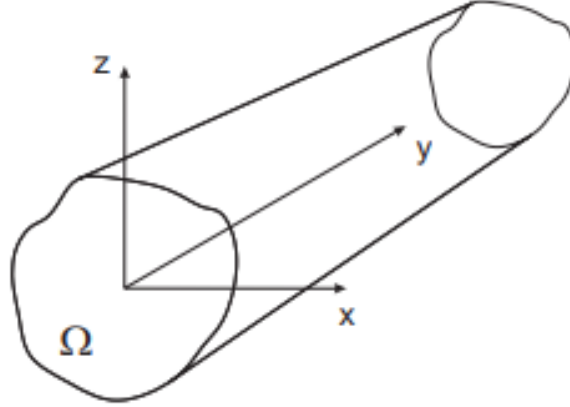


Figure 2.1: Geometry and adopted reference system [19].

As both the strain and stress tensors are symmetric, they may be represented in vector form using Voigt's notation as follows:

$$\boldsymbol{\epsilon} = \{\epsilon_{xx}, \epsilon_{yy}, \epsilon_{zz}, 2\gamma_{xz}, 2\gamma_{yz}, 2\gamma_{xy}\}^T = \{\epsilon_{xx}, \epsilon_{yy}, \epsilon_{zz}, \epsilon_{xz}, \epsilon_{yz}, \epsilon_{xy}\}^T \quad (2.2)$$

$$\boldsymbol{\sigma} = \{\sigma_{xx}, \sigma_{yy}, \sigma_{zz}, \sigma_{yz}, \sigma_{xz}, \sigma_{xy}\}^T \quad (2.3)$$

When dealing with large displacements/rotations of highly flexible structures, accurate definitions of strains and stresses are needed to carry out reliable nonlinear analyses. The Lagrangian formulations are typically used in pure geometrically nonlinear analyses. Two incremental Lagrangian formulations are adopted to compute the deformation and stress states in continuum problems: 1. the total Lagrangian (TL) formulation and 2. the updated Lagrangian (UL) formulation. In detail, in the first approach, strains are written in terms of the undeformed configuration. In the second approach, strains are expressed as a function of deformed configurations in the UL approach [20]. A detailed description of the many advantages of adopting a Lagrangian method is given in Pai's book [21].

Regarding the geometrical relations, the Green-Lagrange strains are taken into consideration. In this manner, the relation between the strains and the displacement can be expressed as

$$\boldsymbol{\epsilon} = (\mathbf{b}_l + \mathbf{b}_{nl}) \mathbf{u} \quad (2.4)$$

where the matrices \mathbf{b}_l and \mathbf{b}_{nl} are the formal matrix of the linear derivatives operator, the complete form of these two matrices are different for 1D and 2D

models and non-linear derivative operators for 1D model defined as follows:

$$\mathbf{b}_l = \begin{bmatrix} \frac{\partial}{\partial x} & 0 & 0 \\ 0 & \frac{\partial}{\partial y} & 0 \\ 0 & 0 & \frac{\partial}{\partial z} \\ \frac{\partial}{\partial z} & 0 & \frac{\partial}{\partial x} \\ \frac{\partial}{\partial z} & \frac{\partial}{\partial y} & 0 \\ 0 & \frac{\partial}{\partial y} & \frac{\partial}{\partial x} \end{bmatrix} \quad \mathbf{b}_{nl} = \begin{bmatrix} \frac{1}{2} \left(\frac{\partial}{\partial x} \right)^2 & \frac{1}{2} \left(\frac{\partial}{\partial x} \right)^2 & \frac{1}{2} \left(\frac{\partial}{\partial x} \right)^2 \\ \frac{1}{2} \left(\frac{\partial}{\partial y} \right)^2 & \frac{1}{2} \left(\frac{\partial}{\partial y} \right)^2 & \frac{1}{2} \left(\frac{\partial}{\partial y} \right)^2 \\ \frac{1}{2} \left(\frac{\partial}{\partial z} \right)^2 & \frac{1}{2} \left(\frac{\partial}{\partial z} \right)^2 & \frac{1}{2} \left(\frac{\partial}{\partial z} \right)^2 \\ \frac{\partial}{\partial x} \frac{\partial}{\partial z} & \frac{\partial}{\partial x} \frac{\partial}{\partial z} & \frac{\partial}{\partial x} \frac{\partial}{\partial z} \\ \frac{\partial y}{\partial} \frac{\partial z}{\partial} & \frac{\partial y}{\partial} \frac{\partial z}{\partial} & \frac{\partial y}{\partial} \frac{\partial z}{\partial} \\ \frac{\partial}{\partial x} \frac{\partial}{\partial y} & \frac{\partial}{\partial x} \frac{\partial}{\partial y} & \frac{\partial}{\partial x} \frac{\partial}{\partial y} \end{bmatrix}$$

where ∂_x stands for the derivative along the x direction, so that $\partial_x = \frac{\partial(\cdot)}{\partial x}$. The same symbol is assumed for y and z directions [22]. For 2D model, The complete Expression of \mathbf{b}_l and \mathbf{b}_{nl} are:

$$\mathbf{b}_l = \begin{bmatrix} \frac{\partial_\alpha}{H_\alpha} & 0 & \frac{1}{H_\alpha R_\alpha} \\ 0 & \frac{\partial_\beta}{H_\beta} & \frac{1}{H_\beta R_\beta} \\ 0 & 0 & \partial_z \\ \partial_z - \frac{1}{H_\alpha R_\alpha} & 0 & \frac{\partial_\alpha}{H_\alpha} \\ 0 & \partial_z - \frac{1}{H_\beta R_\beta} & \frac{\partial_\beta}{H_\beta} \\ \frac{\partial_\beta}{H_\beta} & \frac{\partial_\alpha}{H_\alpha} & 0 \end{bmatrix}$$

$$\mathbf{b}_{nl} = \begin{bmatrix} \frac{1}{2H_\alpha^2} \left((\partial_\alpha)^2 + \frac{2u_z \partial_\alpha}{R_\alpha} + \frac{u_\alpha}{R_\alpha^2} \right) & \frac{(\partial_\alpha)^2}{2H_\alpha^2} & \frac{1}{2H_\alpha^2} \left((\partial_\alpha)^2 - \frac{2u_\alpha \partial_\alpha}{R_\alpha} + \frac{u_z}{R_\alpha^2} \right) \\ \frac{(\partial_\beta)^2}{2H_\beta^2} & \frac{1}{2H_\beta^2} \left((\partial_\beta)^2 + \frac{2u_z \partial_\beta}{R_\beta} + \frac{u_\beta}{R_\beta^2} \right) & \frac{1}{2H_\beta^2} \left((\partial_\beta)^2 - \frac{2u_\beta \partial_\beta}{R_\beta} + \frac{u_z}{R_\beta^2} \right) \\ \frac{1}{2} (\partial_z)^2 & \frac{1}{2} (\partial_z)^2 & \frac{1}{2} (\partial_z)^2 \\ \frac{1}{H_\alpha} \left(\partial_\alpha \partial_z + \frac{u_z \partial_z}{R_\alpha} \right) & \frac{\partial_\alpha \partial_z}{H_\alpha} & \frac{1}{H_\alpha} \left(\partial_\alpha \partial_z - \frac{u_z \partial_z}{R_\alpha} \right) \\ \frac{\partial_\beta \partial_z}{H_\beta} & \frac{1}{H_\beta} \left(\partial_\beta \partial_z + \frac{u_z \partial_z}{R_\beta} \right) & \frac{1}{H_\beta} \left(\partial_\beta \partial_z - \frac{u_\beta \partial_z}{R_\beta} \right) \\ \frac{1}{H_\alpha H_\beta} \left(\partial_\alpha \partial_\beta + \frac{u_z \partial_\beta}{R_\alpha} + \frac{u_\beta}{R_\alpha R_\beta} \right) & \frac{1}{H_\alpha H_\beta} \left(\partial_\alpha \partial_\beta + \frac{u_z \partial_\beta}{R_\beta} \right) & \frac{1}{H_\alpha H_\beta} \left(\partial_\alpha \partial_\beta - \frac{u_\alpha \partial_\beta}{R_\beta} - \frac{u_\beta \partial_\alpha}{R_\beta} \right) \end{bmatrix}$$

where $H_\alpha = \left(1 + \frac{z}{R_\alpha}\right)$, and $H_\beta = \left(1 + \frac{z}{R_\beta}\right)$.

2.1.2 Constitutive equation

The present work focuses on constitutive linear elastic materials to obtain stress components. The constitutive equation in Voigt's notation can be expressed as:

$$\boldsymbol{\sigma} = \mathbf{C}\boldsymbol{\epsilon} \quad (2.5)$$

where \mathbf{C} is the symmetric elasticity tensor defined as:

$$\mathbf{C} = \begin{bmatrix} C_{11} & C_{12} & C_{13} & C_{14} & C_{15} & C_{16} \\ C_{12} & C_{22} & C_{23} & C_{24} & C_{25} & C_{26} \\ C_{13} & C_{23} & C_{33} & C_{34} & C_{35} & C_{36} \\ C_{14} & C_{24} & C_{34} & C_{44} & C_{45} & C_{46} \\ C_{15} & C_{25} & C_{35} & C_{45} & C_{55} & C_{56} \\ C_{16} & C_{26} & C_{36} & C_{46} & C_{56} & C_{66} \end{bmatrix} \quad (3.1.6)$$

In the current work, predominantly isotropic materials are addressed; in this particular scenario, the elasticity tensor assumes a simpler equation based solely on two constants:

$$\mathbf{C} = \begin{bmatrix} C_{11} & C_{12} & C_{12} & 0 & 0 & 0 \\ C_{12} & C_{11} & C_{12} & 0 & 0 & 0 \\ C_{12} & C_{12} & C_{11} & 0 & 0 & 0 \\ 0 & 0 & 0 & C_{44} & 0 & 0 \\ 0 & 0 & 0 & 0 & C_{44} & 0 \\ 0 & 0 & 0 & 0 & 0 & C_{44} \end{bmatrix} \quad (2.6)$$

In which each component is expressed in terms of Lamé parameters, Young's modulus, and Poisson's coefficient.

$$C_{11} = C_{22} = C_{33} = 2G + \lambda; \quad C_{12} = C_{13} = C_{23} = \lambda; \quad C_{44} = C_{55} = C_{66} = G; \quad (2.7)$$

$$G = \frac{E}{2(1 + \nu)}; \quad \lambda = \frac{\nu E}{(1 + \nu)(1 - 2\nu)} \quad (2.8)$$

For completeness, the elasticity tensor for orthotropic materials (with a primary direction) is presented. The properties of the fiber in the transversal direction differ from those in the main direction; therefore, Young moduli and additional coefficients must be defined for each direction [23]. The elasticity tensor takes this form:

$$\mathbf{C} = \begin{bmatrix} C_{11} & C_{12} & C_{13} & 0 & 0 & 0 \\ C_{21} & C_{22} & C_{23} & 0 & 0 & 0 \\ C_{31} & C_{32} & C_{33} & 0 & 0 & 0 \\ 0 & 0 & 0 & C_{44} & 0 & 0 \\ 0 & 0 & 0 & 0 & C_{55} & 0 \\ 0 & 0 & 0 & 0 & 0 & C_{66} \end{bmatrix} \quad (2.9)$$

The generic element of the elasticity tensor will be function of (in general) all this coefficient just defined:

$$C_{ij} = C_{ij}(E_1, E_2, E_3, G_{23}, G_{13}, G_{12}, \nu_{23}, \nu_{13}, \nu_{12}) \quad (2.10)$$

Coefficients C_{ij} depend on Young and Poisson moduli as well as on the fiber orientation angle θ that is graphically defined in Figure 2.2 where 1,2,3 represents the axis of the material.

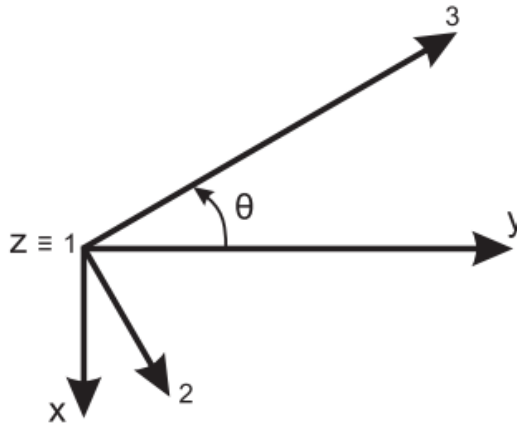


Figure 2.2: Fiber Orientation angle [19].

The prior expression refers to the material reference frame. To represent the same elasticity tensor in the global reference frame, use the following rotation:

$$\mathbf{T} = \begin{bmatrix} \cos^2 \theta & \sin^2 \theta & 0 & 0 & 0 & -\sin 2\theta \\ \sin^2 \theta & \cos^2 \theta & 0 & 0 & 0 & \sin 2\theta \\ 0 & 0 & 1 & 0 & 0 & 0 \\ 0 & 0 & 0 & \cos \theta & \sin \theta & 0 \\ 0 & 0 & 0 & -\sin \theta & \cos \theta & 0 \\ \sin \theta \cos \theta & -\sin \theta \cos \theta & 0 & 0 & 0 & \cos 2\theta \end{bmatrix} \quad (2.11)$$

Applying this rotation, Hooke's law written in the global ref. frame becomes:

$$\sigma = \mathbf{T}^T \mathbf{C} \mathbf{T} \varepsilon = \mathbf{Q} \varepsilon \quad (2.12)$$

Where the compact global matrix is:

$$\mathbf{Q} = \begin{bmatrix} Q_{11} & Q_{12} & Q_{13} & 0 & 0 & Q_{16} \\ Q_{21} & Q_{22} & Q_{23} & 0 & 0 & Q_{26} \\ Q_{31} & Q_{32} & Q_{33} & 0 & 0 & Q_{36} \\ 0 & 0 & 0 & Q_{44} & Q_{45} & 0 \\ 0 & 0 & 0 & Q_{54} & Q_{55} & 0 \\ Q_{16} & Q_{26} & Q_{36} & 0 & 0 & Q_{66} \end{bmatrix} \quad (2.13)$$

For the sake of brevity, the expressions for the components of the matrix \mathbf{Q} are not reported here, but can be referred to in [23],[24] . Furthermore, it should be noted that models with constant and linear distributions of the in-plane displacement components u_x and u_z , are require modified material coefficients to overcome Poisson locking [25].

2.2 Carrera Unified Formulation approach

In the last years, different theories have been implemented within the CUF framework. Thanks to their capabilities, polynomial expression have been mostly used in CUF-based analyses [26]. According to Carrera Unified Formulation, the displacement field is expressed as an expansion of fundamental polynomial terms, with the order of expansion increasing as needed. The displacement field is then written as a combination of the finite element's nodal displacements, and it varies depending on the model used: in 1D CUF models, thickness functions are used to approximate the displacement field along the cross-section of the beam, whereas in 2D models, thickness functions are used to approximate the displacement field along the thickness of the plate. The choice of cross-section/thickness expansion function is entirely arbitrary, but it characterizes the model used: when Taylor polynomials are used, structure is solved by considering an equivalent single layer for the entire cross-section (ESL models), whereas when Lagrange polynomials are used, a Layer-Wise description of the displacement field is permitted (LW models).

2.2.1 Beam 1D CUF-FEM Finite Element

Consider beam and plate models described in a Cartesian reference frame (x, y, z) . 1D CUF models are used in elongated structures, specifically beam constructions, where the characteristic length is significantly bigger than the cross-section dimensions. In this model, the 3D displacement field's major variables are discretized along the axis using a traditional FEM approximation, which is then utilized to interpolate the nodal cross-section displacement components. The derivation of the following

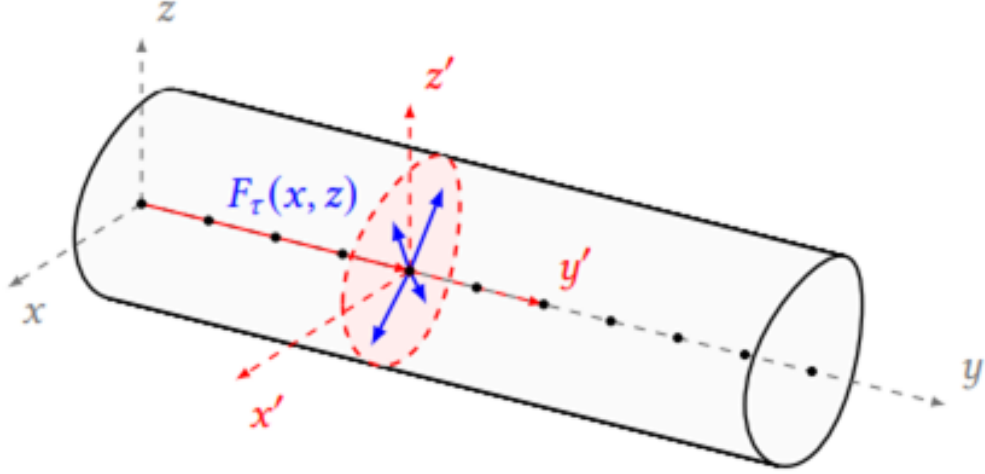


Figure 2.3: Beam structure.

theoretical formulation is independent of the choice of the cross-section or thickness [16]. If y is the direction of the beam axis and x', z' is the reference plane for the cross-section, according to Carrera Unified Formulation The 3D stationary displacement field of an arbitrary point within the structural domain can be expressed as follows:

$$\mathbf{u}(x, y, z) = F_\tau(x, z)\mathbf{u}_\tau(y) = F_\tau(x, z)N_i(y)q_{ri} \quad \tau = 1, 2, \dots, K \quad (2.14)$$

where $F_\tau(x, z)$ are the cross-section expansion functions, K is the order of expansion in the thickness direction. The indexes τ stand for the summing convention q_{ri} are the nodal discrete displacements and $N_i(y)$ are the classical 1D shape functions involved in FEM used for the approximation along the beam axis. The choice of F_τ is purely arbitrary and determines the theory of structure adopted for a given problem. In the context of geometrically non-linear elasticity, the geometrical relations can be rewritten as:

$$\epsilon = (\mathbf{b}_l + \mathbf{b}_{nl})\mathbf{u} = (\mathbf{b}_l + \mathbf{b}_{nl})F_\tau(x, z)N_i(y)q_{ri} = (\mathbf{B}_1^{\tau i} + \mathbf{B}_{nl}^{\tau i})q_{ri} \quad (2.15)$$

where $\mathbf{B}_1^{\tau i}$ and $\mathbf{B}_{nl}^{\tau i}$ are the formal matrices of derivatives operators applied to shape functions and cross-section functions, that can be rewritten then as:

$$\mathbf{B}_1^{\tau i} = \begin{bmatrix} F_{\tau,x}N_i & 0 & 0 \\ 0 & F_{\tau}N_{i,y} & 0 \\ 0 & 0 & F_{\tau,z}N_i \\ F_{\tau,z}N_i & 0 & F_{\tau,x}N_i \\ 0 & F_{\tau,z}N_i & F_{\tau}N_{i,y} \\ F_{\tau}N_{i,y} & F_{\tau,x}N_i & 0 \end{bmatrix} \quad (2.16)$$

$$\mathbf{B}_{nl}^{\tau i} = \frac{1}{2} \begin{bmatrix} u_{x,x}F_{\tau,x}N_i & u_{y,x}F_{\tau,x}N_i & u_{z,x}F_{\tau,x}N_i \\ u_{x,y}F_{\tau}N_{i,y} & u_{y,y}F_{\tau}N_{i,y} & u_{z,y}F_{\tau}N_{i,y} \\ u_{x,z}F_{\tau,z}N_i & u_{y,z}F_{\tau,z}N_i & u_{z,z}F_{\tau,z}N_i \\ u_{x,x}F_{\tau,z}N_i + u_{x,z}F_{\tau,x}N_i & u_{y,x}F_{\tau,z}N_i + u_{y,z}F_{\tau,x}N_i & u_{z,x}F_{\tau,z}N_i + u_{z,z}F_{\tau,x}N_i \\ u_{x,y}F_{\tau,z}N_i + u_{x,z}F_{\tau}N_{i,y} & u_{y,y}F_{\tau,z}N_i + u_{y,z}F_{\tau}N_{i,y} & u_{z,y}F_{\tau,z}N_i + u_{z,z}F_{\tau}N_{i,y} \\ u_{x,x}F_{\tau}N_{i,y} + u_{x,y}F_{\tau,x}N_i & u_{y,x}F_{\tau}N_{i,y} + u_{y,y}F_{\tau,x}N_i & u_{z,x}F_{\tau}N_{i,y} + u_{z,y}F_{\tau,x}N_i \end{bmatrix} \quad (2.17)$$

2.2.2 Plate 2D CUF-FEM Finite Element

In structures where only the thickness is at least one order of dimension less than the other dimensions, 2D CUF models are adopted. In this model, the primary variables of the 3D displacement field are expressed adopting through-the-thickness expansion of finite nodes on the mid-surface of the plate, already discretized by a classical FEM approximation. If z is the thickness direction, and x, y is the reference plane for the mid-surface of the plate, according to Carrera Unified Formulation the displacement field is written as:

$$\mathbf{u}(x, y, z) = \mathbf{F}_{\tau}(z)\mathbf{u}_{\tau}(x, y) = \mathbf{F}_{\tau}(x)N_i(x, y)q_{ri} \quad \tau = 1, 2, \dots, K \quad (2.18)$$

where $F_{\tau}(z)$ are the thickness expansion function, used for the approximation of the displacement field along the thickness, K is the order of expansion, q_{ri} are the nodal discrete displacements and $N_i(x, y)$ are the classical 2D shape functions involved in FEM used for the approximation of the displacement field along the mid-surface. In the context of geometrically non linear elasticity, the geometrical relations can be rewritten as:

$$\boldsymbol{\epsilon} = (b_l + b_{nl})\mathbf{u} = (b_l + b_{nl})F_{\tau}(x, z)N_i(y)q_{ri} = (\mathbf{B}_1^{r_i} + \mathbf{B}_{nl}^{r_i})q_{ri} \quad (2.19)$$

Where $B_1^{r_i}$ and $B_{nl}^{r_i}$ are the formal matrices of derivatives operators applied to

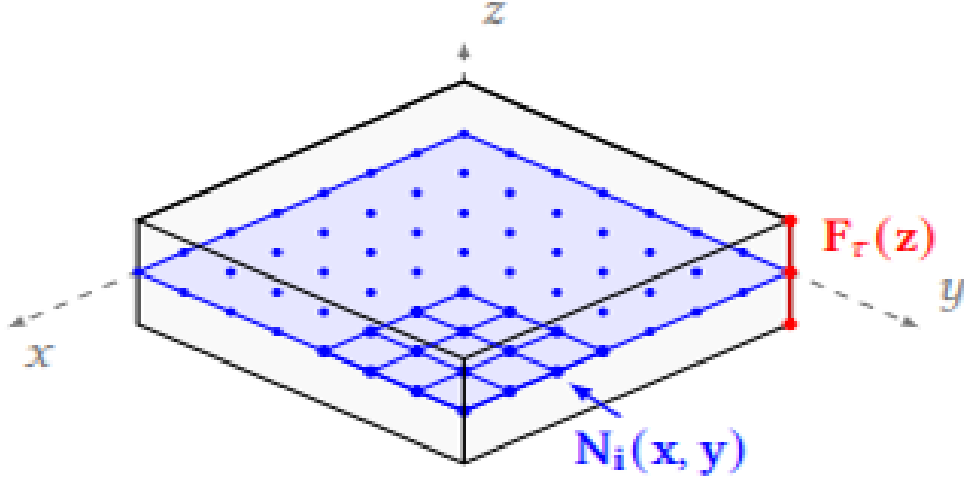


Figure 2.4: Plate 2D model.

shape functions and thickness function that can be rewritten then as:

$$\mathbf{B}_1^{r_i} = \begin{bmatrix} F_\tau N_{i,x} & 0 & 0 \\ 0 & F_\tau N_{i,y} & 0 \\ 0 & 0 & F_{\tau,z} N_i \\ F_{\tau,z} N_i & 0 & F_\tau N_{i,x} \\ 0 & F_{\tau,z} N_i & F_\tau N_{i,y} \\ F_\tau N_{i,y} & F_\tau N_{i,x} & 0 \end{bmatrix} \quad (2.20)$$

$$\mathbf{B}_{nl}^{r_i} = \frac{1}{2} \begin{bmatrix} u_{x,x} F_\tau N_{i,x} & u_{y,x} F_\tau N_{i,x} & u_{z,x} F_\tau N_{i,x} \\ u_{x,y} F_\tau N_{i,y} & u_{y,y} F_\tau N_{i,y} & u_{z,y} F_\tau N_{i,y} \\ u_{x,z} F_{\tau,z} N_i & u_{y,z} F_{\tau,z} N_i & u_{z,z} F_{\tau,z} N_i \\ u_{x,x} F_{\tau,z} N_i + u_{x,z} F_\tau N_{i,x} & u_{y,x} F_{\tau,z} N_i + u_{y,z} F_\tau N_{i,x} & u_{z,x} F_{\tau,z} N_i + u_{z,z} F_\tau N_{i,x} \\ u_{x,y} F_{\tau,z} N_i + u_{x,z} F_\tau N_{i,y} & u_{y,y} F_{\tau,z} N_i + u_{y,z} F_\tau N_{i,y} & u_{z,y} F_{\tau,z} N_i + u_{z,z} F_\tau N_{i,y} \\ u_{x,x} F_\tau N_{i,y} + u_{x,y} F_\tau N_{i,x} & u_{y,y} F_\tau N_{i,y} + u_{y,y} F_\tau N_{i,x} & u_{z,x} F_\tau N_{i,y} + u_{z,y} F_\tau N_{i,x} \end{bmatrix} \quad (2.21)$$

2.2.3 Taylor Expansion Model

According to Carrera Unified Formulation (CUF), the generic displacement field can be expressed in a compact manner as an expansion in terms of arbitrary functions, F_τ , [19]

$$\mathbf{u}(x, y, z) = F_\tau(x, z) \mathbf{u}_\tau(y), \quad \tau = 1, 2, \dots, M \quad (2.22)$$

where F_τ are the functions of the coordinates x and z on the cross-section; \mathbf{u}_τ is the vector of the generalized displacements; M stands for the number of terms used in the expansion; and the repeated subscript, τ , indicates summation. The choice of F_τ determines the class of the 1D CUF model.

Taylor Expansion (TE) 1D CUF models consist of MacLaurin series that uses the 2D polynomials $x^i z^j$ as F_τ basis. Table 2.1 shows M and F_τ as functions of the expansion order, N , which represents the maximum order of the polynomials used in the expansion.

According to CUF, Eqs. (2.7) to (2.11) consist of particular cases of TE theories. For example, it should be noted that Eqs. (2.7), (2.8), and (2.10) are degenerated cases of the linear ($N = 1$) TE model, which can be expressed as:

$$\begin{aligned} u_x &= u_{x1} + x u_{x2} + z u_{x3}, \\ u_y &= u_{y1} + x u_{y2} + z u_{y3}, \\ u_z &= u_{z1} + x u_{z2} + z u_{z3}. \end{aligned} \tag{2.23}$$

where the parameters on the right-hand side ($u_{x1}, u_{y1}, u_{z1}, u_{x2}$, etc.) are the displacements of the beam axis and first derivatives of displacements. Higher order terms can be taken into account according to Eq.(2.22).

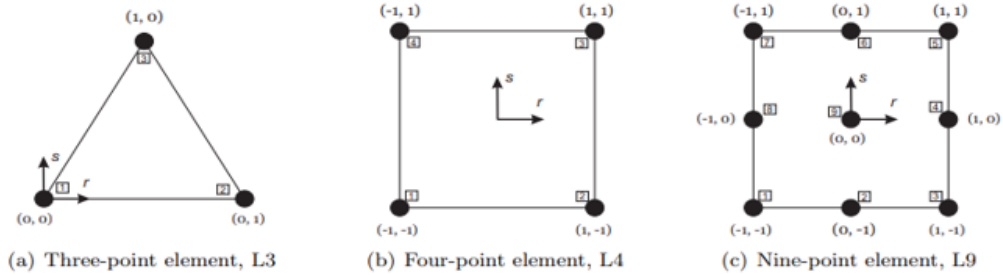


Figure 2.5: Cross section L-elements in natural geometry.

2.2.4 Lagrange Expansion Model

Lagrange Expansion (LE) models use Lagrange polynomials to interpolate displacement variables: in 1D/2D models, unknowns over the cross-section/thickness domain are interpolated, whereas in 3D models, the displacement field is expressed as an expansion over all the unknown nodal displacements of the finite element. In the code, different LE orders elements are implemented for 1D/2D elements, namely Q4 (four node element), Q9 (nine node element), and Q16 (sixteen node element); in the case of 3D LE elements, instead H8 (eight node element), H20

(twenty node element), and H27 (twenty-seven node element) are implemented. [23]. In general, the expansion is defined in the natural reference frame: each polynomial is defined in the real interval $[-1, 1]$: physical quantities depending on the Lagrange expansions need a change of variable where the Jacobian is required.

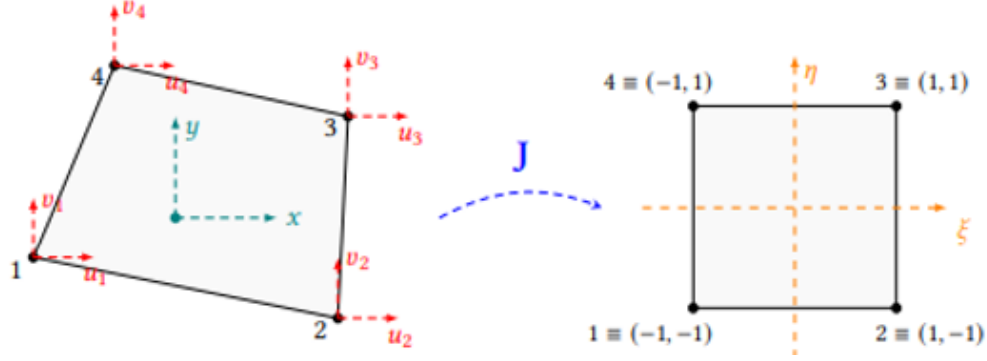


Figure 2.6: Lagrange Q4 linear phase element: from material to natural ref.frame.

As an example, in the case of linear Q4 element as shown in Figure. 2.6, Lagrange polynomials in the natural reference frame are expressed as follows:

$$N_1(\xi, \eta) = \frac{1}{4}(1 - \xi)(1 - \eta) \quad (2.24)$$

$$N_2(\xi, \eta) = \frac{1}{4}(1 + \xi)(1 - \eta) \quad (2.25)$$

$$N_3(\xi, \eta) = \frac{1}{4}(1 + \xi)(1 + \eta) \quad (2.26)$$

$$N_4(\xi, \eta) = \frac{1}{4}(1 - \xi)(1 + \eta) \quad (2.27)$$

Therefore, once the nodal displacements are computed, the displacement field of a Q4 domain in the physical reference frame is written as:

$$u_x = N_1u_{x_1} + N_2u_{x_2} + N_3u_{x_3} + N_4u_{x_4} \quad (2.28)$$

$$u_y = N_1u_{y_1} + N_2u_{y_2} + N_3u_{y_3} + N_4u_{y_4} \quad (2.29)$$

$$u_z = N_1u_{z_1} + N_2u_{z_2} + N_3u_{z_3} + N_4u_{z_4} \quad (2.30)$$

2.3 Failure Analysis

Composites offer remarkable mechanical strength and lightweight properties, making them an appealing option for structural applications with the potential to enhance performance and increase efficiency. However, despite these numerous benefits, composites can present challenges due to their complex nature and heterogeneous composition, which makes understanding their failure mechanisms more difficult. The analysis of failures in composite materials is significantly more complicated than in isotropic materials. This added complexity is due to their orthotropic behavior and the existence of multiple possible failure modes, including fibre and matrix failures. There are numerous criteria available to assess and, in some cases, predict various failure modes. This chapter delves into the failure analysis of composites using a range of independent and polynomial criteria [10], [27]

2.3.1 Failure criteria

Different failure criteria are employed to estimate the strength of materials and systems under multiaxial loading conditions. These criteria define a relationship between the material's strength limits, which are usually identified for uniaxial tension, compression, and shear, and the overall stress-strain state caused by multiaxial loads. Failure criteria are often expressed through mathematical formulas known as failure criterion functions (f), which are based on stresses (or strains) and the material's strength parameters [10].

2.3.2 Maximum Stress Criterion

The Maximum Stress criterion (MS) does not consider any interaction between different stress components. It is based on the concept that the failure occurs when the stress in at least one direction exceeds the correspondent critical value [28]. This theory, like Rankine's maximum normal stress theory and Tresca's maximum shearing stress theory, applies to isotropic materials [29]. Stresses on a lamina are divided into normal and shear stresses on the local axes.

The conditions for the MS of an anisotropic material can be summed up as follows :

$$\begin{aligned}
 & \sigma_{11} \geq 0 \Rightarrow \sigma_{11} \geq X_T \\
 \text{or } & \sigma_{11} < 0 \Rightarrow \sigma_{11} \leq X_C \\
 & \sigma_{22} \geq 0 \Rightarrow \sigma_{22} \geq Y_T \\
 \text{or } & \sigma_{22} < 0 \Rightarrow \sigma_{22} \leq Y_C \\
 & \sigma_{33} \geq 0 \Rightarrow \sigma_{33} \geq Z_T \\
 \text{or } & \sigma_{33} < 0 \Rightarrow \sigma_{33} \leq Z_C \\
 & \tau_{12} \geq S_{12}^L \\
 & \tau_{13} \geq S_{13}^L \\
 & \tau_{23} \geq S_{23}^L
 \end{aligned} \tag{2.31}$$

where X , Y , and Z are respectively the strength parameter in 1-, 2-, and 3-directions. X , Y , and Z can also be addressed as "Failure Coefficients", FC . For anisotropic materials, these parameters are different depending on the direction. Furthermore, different values can be found for traction or compression loadings; the superscripts T, C indicate the corresponding values in the axial traction and compression cases, while the superscript L indicates a strength parameter in a shear direction. In particular, if anisotropic materials are taken into account, for the shear case three different strength values have to be considered, $L_1 = 12$, $L_2 = 13$, $L_3 = 23$. For the Maximum Stress criterion, the FI is obtained as follows, points in which the index becomes greater or equal to one indicate that failure occurred [30].

$$FI = \max \left[\frac{\sigma_{ij}}{FC^{T,C}} \right] \tag{2.32}$$

2.3.3 Tsai-Wu Criterion

The Tsai-Wu (TW) is a quadratic interaction tensor polynomial failure criterion. This criterion was theoretically formulated starting from the basic assumption that there exists a failure surface in the stress-space in the following scalar form:

$$f(\sigma_k) = F_i \sigma_i + F_{ij} \sigma_i \sigma_j = 1 \quad i, j, k = 1, \dots, 6 \tag{2.33}$$

where F_i and F_{ij} are strength tensors respectively of second and fourth orders. In this criterion, the linear part, σ_i , takes into account the difference between the sign of the stress who induces the failure while the quadratic term, $\sigma_i \sigma_j$, defines an ellipsoid in the stress space [31]. By expanding Equation 6.8, the criterion becomes:

$$\begin{aligned}
 & A_{11}\sigma_{11}^2 + A_{22}\sigma_{22}^2 + A_{33}\sigma_{33}^2 + B_1\sigma_{11} + B_2\sigma_{22} + B_3\sigma_{33} + 2A_{12}\sigma_{11}\sigma_{22} \\
 & + 2A_{13}\sigma_{11}\sigma_{33} + 2A_{23}\sigma_{22}\sigma_{33} + A_{66}\tau_{12}^2 + A_{55}\tau_{13}^2 + A_{44}\tau_{23}^2 \geq 1
 \end{aligned} \tag{2.34}$$

where the coefficients, A_{11}, \dots, A_{66} reported in Equation 2.35 can be obtained as:

$$\begin{aligned}
 A_{11} &= \frac{1}{X^T X^C} \\
 A_{22} &= \frac{1}{Y^T Y^C} \\
 A_{33} &= \frac{1}{Z^T Z^C} \\
 B_1 &= \frac{1}{X^T} - \frac{1}{X^C} \\
 B_2 &= \frac{1}{Y^T} - \frac{1}{Y^C} \\
 B_3 &= \frac{1}{Z^T} - \frac{1}{Z^C} \\
 A_{12} &= \frac{1}{2\sqrt{X^T X^C Y^T Y^C}} \\
 A_{13} &= \frac{1}{2\sqrt{X^T X^C Z^T Z^C}} \\
 A_{23} &= \frac{1}{2\sqrt{Y^T Y^C Z^T Z^C}} \\
 A_{44} = A_{55} = A_{66} &= \frac{1}{S^L S^L}
 \end{aligned} \tag{2.35}$$

2.3.4 Tsai-Hill Criterion

The Tsai-Hill (TH) is an interactive quadratic criterion. It represents the extension to composites of the Von Mises criterion used to analyse metals. This criterion was formulated by referring to distortional energy. It is known that total strain energy in a body is composed of two parts: the distortion energy which cause change in shape and the second that is a dilation energy which causes the change in size or volume. In the Von Mises criterion it is assumed that the material fails when the maximum distortion energy of the body exceeds the distortion energy corresponding to yielding of the same material in tension. Hill extended the von Mises distortion energy criterion of isotropic materials to anisotropic materials; later Tsai extended this criterion for anisotropic materials to unidirectional laminae.

$$\begin{aligned}
 \left(\frac{\sigma_{11}}{X}\right)^2 + \left(\frac{\sigma_{22}}{Y}\right)^2 + \left(\frac{\sigma_{33}}{Z}\right)^2 - A\sigma_{11}\sigma_{22} - B\sigma_{11}\sigma_{33} - C\sigma_{22}\sigma_{33} + \\
 \left(\frac{\sigma_{23}}{S_{23}}\right)^2 + \left(\frac{\sigma_{31}}{S_{13}}\right)^2 + \left(\frac{\sigma_{12}}{S_{12}}\right)^2 \geq 1
 \end{aligned} \tag{2.36}$$

$$\begin{aligned} A &= \frac{1}{X^2} + \frac{1}{Y^2} - \frac{1}{Z^2} \\ B &= \frac{1}{X^2} - \frac{1}{Y^2} + \frac{1}{Z^2} \\ C &= \frac{1}{Y^2} + \frac{1}{Z^2} - \frac{1}{X^2} \end{aligned} \tag{2.37}$$

Chapter 3

Analysis

3.1 Analysis Using Abaqus

The 3D model of the component was initially developed using specialized design software and subsequently imported into Abaqus for advanced analysis. Once the model was successfully imported, the next step involved assigning material properties.

To enhance the precision of the analysis, a structured mesh was generated for the model. Structured meshing was selected because it provides a more uniform and organized grid, leading to higher accuracy in the results, especially in critical areas of the model.

Following the meshing process, boundary conditions were applied based on the specific requirements of the analysis. At one end of the model, both rotational and deformation movements were constrained to simulate the actual operational conditions of the structure and the other end was completely free.

The load conditions were then applied, determined by the most critical point identified from the flight envelope [32], known as the maximum manoeuvre point. The flight envelope is a plot that illustrates the relationship between load factor and airspeed, including important curves such as the stall curve and the maximum load factor curve. The intersection of these two curves defines the maximum manoeuvre point, which represents the most critical aerodynamic and structural conditions the aircraft might encounter during flight. At this point, all the relevant loads were calculated using the numerical model, reflecting the extreme operating conditions that the structure must endure.

These loading conditions, along with the defined constraints and boundary conditions, were thoroughly depicted in the accompanying figure 3.1, 3.2, 3.3, 3.4, 3.5. After setting up the model with all these parameters, the analysis was conducted to evaluate the maximum displacement of the central wing box when subjected

to these conditions, considering different material scenarios. This comprehensive approach ensures that the structural integrity of the wing box is thoroughly assessed under the most demanding operational circumstances.

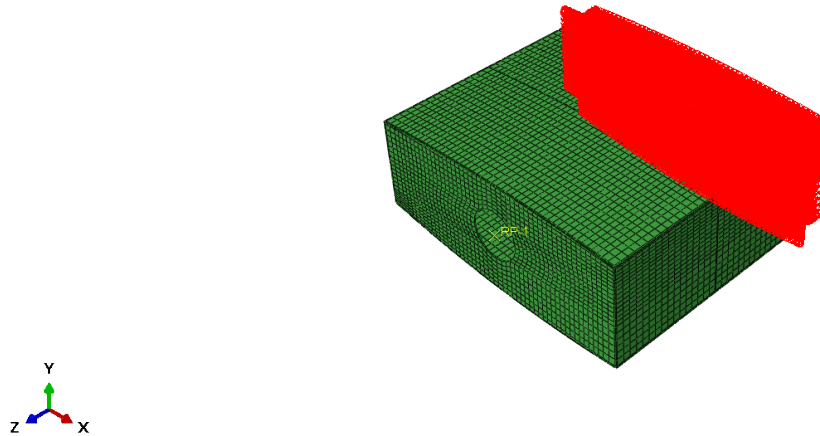


Figure 3.1: Boundary Condition.

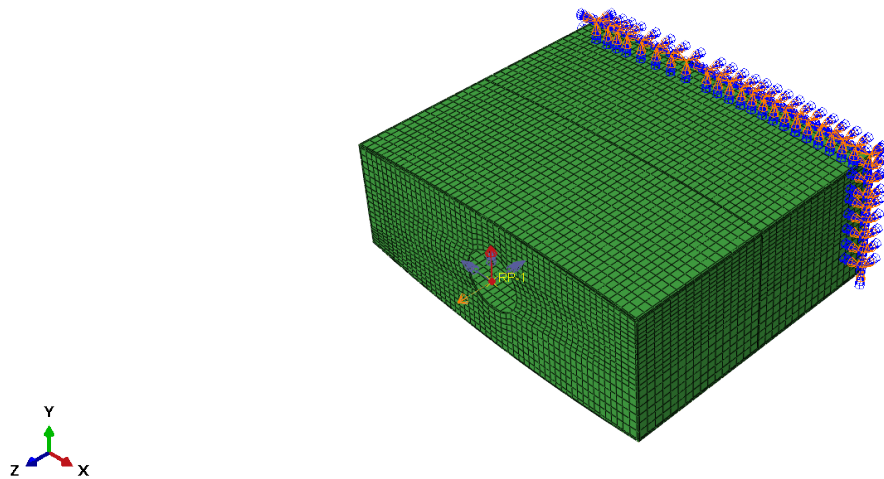


Figure 3.2: Load Condition 1.

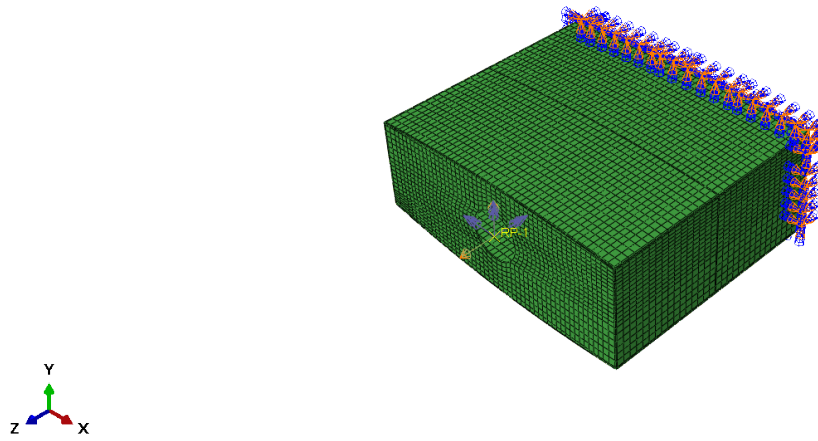


Figure 3.3: Load Condition 2.

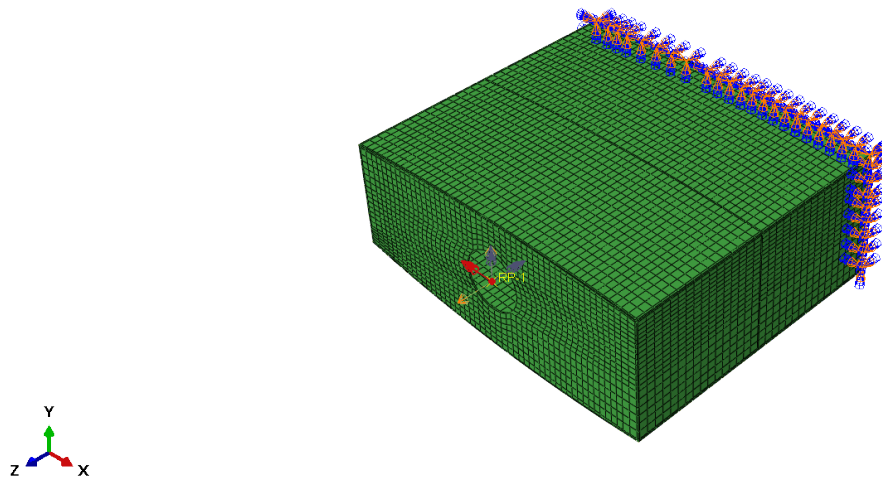


Figure 3.4: Load Condition 3.

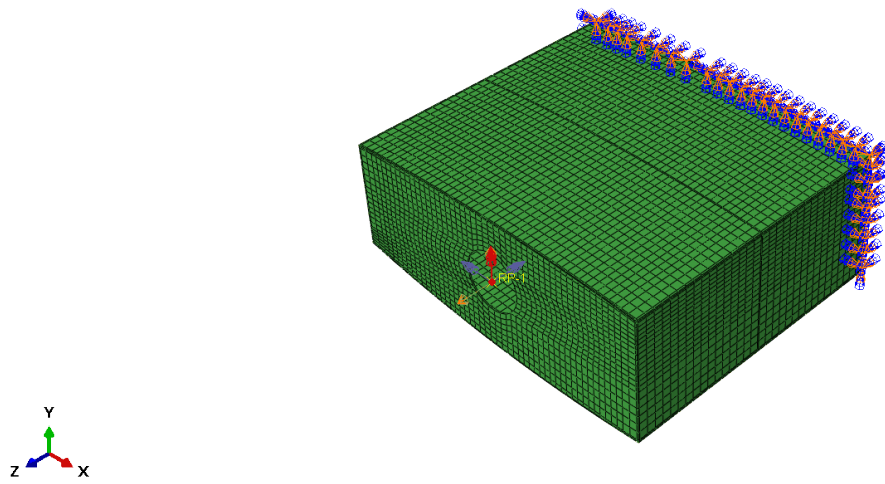


Figure 3.5: Load Condition 4.

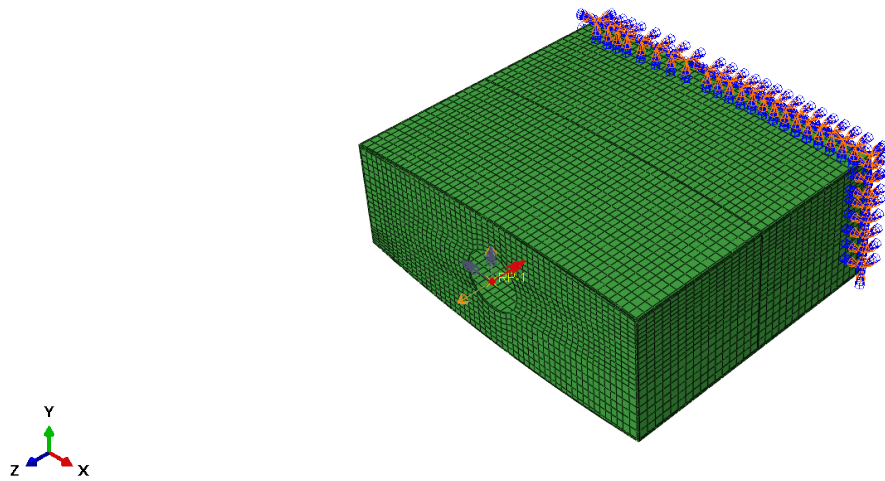


Figure 3.6: Load Condition 5.

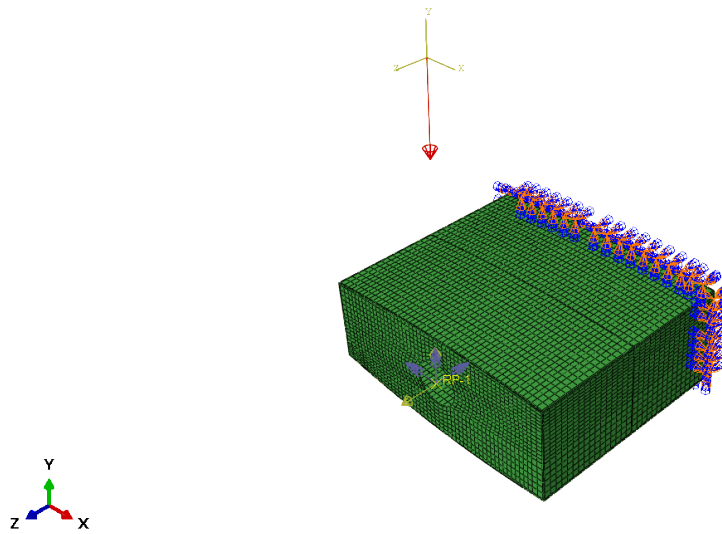


Figure 3.7: Gravity.

3.2 Analysis Using CUF

For the CUF (Carrera Unified Formulation) analysis, we utilized an executable file to perform the necessary computations. The process involved several important steps to ensure the analysis was conducted accurately. First and foremost, it was essential to organize all the input files correctly, following a specific order as depicted in the accompanying figure. This organization is crucial because it allows the executable to correctly interpret and utilize the data for the analysis. Within this setup, the `PATH_Input` variable plays a vital role. This variable is configured to include the path addresses of all relevant files associated with the analysis. By specifying these path addresses, `PATH_Input` ensures that the executable file can accurately locate and read all the files required for the analysis process, regardless of their location in the directory structure. This meticulous setup is crucial for the successful execution of the CUF analysis, as it guarantees that all components of the analysis are accessible and correctly integrated, allowing for a smooth and error-free computational process.

Deepak - Personal > Desktop > MUL code > CUF_20240131_101

Sort View

Name	Type	Size
ANALYSIS	DAT File	1 KB
BC	DAT File	233 KB
CONNECTIVITY	DAT File	2 KB
EXP_CONN_01	DAT File	35 KB
EXP_CONN_02	DAT File	5 KB
EXP_CONN_03	DAT File	35 KB
EXP_MESH_01	DAT File	65 KB
EXP_MESH_02	DAT File	16 KB
EXP_MESH_03	DAT File	65 KB
FREQ_RESP	DAT File	1 KB
LAMINATION	DAT File	1 KB
MATERIAL	DAT File	1 KB
NODES	DAT File	3 KB
PBC	DAT File	1 KB
POSTPROCESSING	DAT File	1 KB
VERSORS	DAT File	1 KB

Figure 3.8: Input Folder

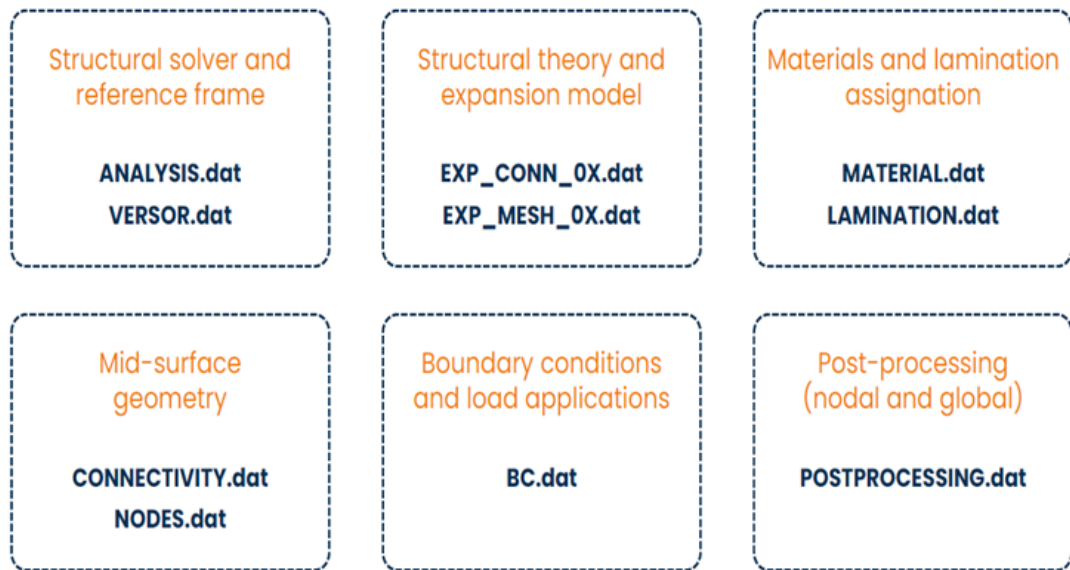


Figure 3.9: Structural Model Requirements

ANALYSIS.dat: This file is used to define the type of analysis to be performed, such as linear static analysis, free vibration analysis, dynamic analysis, thermo-mechanical analysis, and others. Each type of analysis is identified by a specific numerical code within the software. For example, a linear static analysis is represented by the code 101, while free vibration analysis is denoted by 103. You select the desired analysis type by specifying its corresponding code in this file.

POSTPROCESSING.dat: In this file, the post-processing parameters are defined. The software outputs the calculated displacements, strains, and stresses at specified points, as listed in this file, into a text document. Additionally, the file allows you to request results formatted for visualization in ParaView, enabling detailed analysis and interpretation of the simulation outcomes.

VERSORS.dat: This file defines the local reference frames for the elements. These reference frames are assigned during the element definition process and are crucial for accurately representing the orientation and behaviour of elements within the global structural framework.

BC.dat: The 'BC.dat' file is where you define both the geometric and mechanical boundary conditions for the analysis. These conditions are specified using a set of predefined commands within the software interface, allowing you to accurately describe how the structure is constrained, supported, and loaded during the analysis.

- **F-POINT:** Concentrated force, located at the node of coordinates x, y, z (it has to be a node of the mesh), expressed in terms of components

- **D-POINT:** One can specify the displacement components of a single node
- **D-PLANE:** One can specify the displacement components for all the points laying on the specified plane
- **F-PRESS:** Surface pressure, applied for all the points on the specified physical surface

Boundary Condition	ID	X	Y	Z	DOF 1	DOF 2	DOF 3
2584							
D-POINT 1	1	2.88569987D-01	0.52760000D+00	-2.52469003D-01	0.000	0.000	0.000
D-POINT 2	2	2.88758606D-01	0.52760000D+00	-2.54962355D-01	0.000	0.000	0.000
D-POINT 3	3	2.91557342D-01	0.52760000D+00	-2.52188265D-01	0.000	0.000	0.000
D-POINT 4	4	2.88947195D-01	0.52760000D+00	-2.57455707D-01	0.000	0.000	0.000
D-POINT 5	5	2.91745931D-01	0.52760000D+00	-2.54681528D-01	0.000	0.000	0.000
D-POINT 6	6	2.91934520D-01	0.52760000D+00	-2.57174820D-01	0.000	0.000	0.000
D-POINT 7	7	3.05002302D-01	0.52760000D+00	-2.50955492D-01	0.000	0.000	0.000
D-POINT 8	8	2.89842814D-01	0.52760000D+00	-2.69296467D-01	0.000	0.000	0.000

Figure 3.10: Boundary Condition.DAT file with D-point.

In the figure 3.10 3.11, the first number indicates the total number of boundary conditions applied to the structure. The first column specifies the type of boundary condition, and in this particular case, it shows that type of boundary conditions have been applied labelled as D and F point. The second column provides the identification (ID) of these points. The third, fourth, and fifth columns represent the coordinates (x, y, z) of these points in the respective directions. The remaining columns detail the specific degrees of freedom that are constrained or restricted at each of these points.

Boundary Condition	ID	X	Y	Z	DOF 1	DOF 2	DOF 3
1303							
F-POINT 1303	1303	3.18451732D-01	0.00000000D+00	-2.49772549D-01	0.000	-1.37600	16.37500
F-POINT 1304	1304	3.18602592D-01	0.00000000D+00	-2.51766950D-01	0.000	-1.37600	16.37500
F-POINT 1305	1305	2.93728560D-01	0.00000000D+00	-2.80893207D-01	0.000	-1.37600	16.37500
F-POINT 1306	1306	3.06282401D-01	0.00000000D+00	-2.67878562D-01	0.000	-1.37600	16.37500
F-POINT 1307	1307	3.18828881D-01	0.00000000D+00	-2.54758567D-01	0.000	-1.37600	16.37500
F-POINT 1308	1308	3.29739332D-01	0.00000000D+00	-2.48818502D-01	0.000	-1.37600	16.37500
F-POINT 1309	1309	2.91634083D-01	0.00000000D+00	-2.92978019D-01	0.000	-1.37600	16.37500
F-POINT 1310	1310	3.29888344D-01	0.00000000D+00	-2.50813007D-01	0.000	-1.37600	16.37500
F-POINT 1311	1311	2.94625580D-01	0.00000000D+00	-2.92752385D-01	0.000	-1.37600	16.37500
F-POINT 1312	1312	3.07185382D-01	0.00000000D+00	-2.79815525D-01	0.000	-1.37600	16.37500
F-POINT 1313	1313	3.19737047D-01	0.00000000D+00	-2.66764939D-01	0.000	-1.37600	16.37500

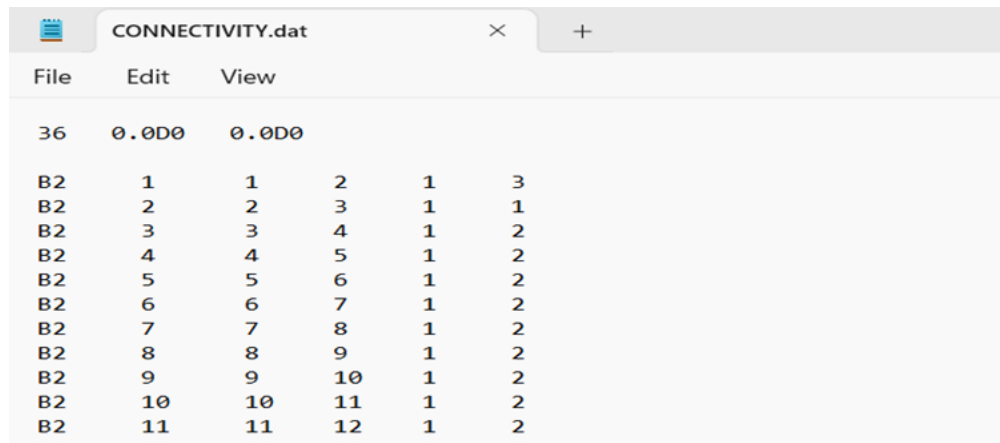
Figure 3.11: Boundary Condition.DAT file with F-point.

In the Carrera Unified Formulation (CUF), when solving a problem, we can choose either the beam approach or the plate approach. In the beam approach, we first model the cross-section of the beam. CUF then extends this cross-section using a Finite Element Method (FEM) approach in the third direction, capturing the beam's behavior in three dimensions. On the other hand, in the plate approach, we start by modeling the thickness of the plate. Here, we design in one dimension, and the CUF automatically expands this model into the other dimensions, effectively capturing the plate's behavior across its surface.

File	Edit	View				
37						
1	0.00000000D+00	0.00000000D+00	0.00000000D+00	LE	1	
2	0.00000000D+00	1.00000000D-04	0.00000000D+00	LE	1	
3	0.00000000D+00	2.60000000D-03	0.00000000D+00	LE	1	
4	0.00000000D+00	1.88500000D-02	0.00000000D+00	LE	1	
5	0.00000000D+00	3.51000000D-02	0.00000000D+00	LE	1	
6	0.00000000D+00	5.13500000D-02	0.00000000D+00	LE	1	
7	0.00000000D+00	6.76000000D-02	0.00000000D+00	LE	1	
8	0.00000000D+00	8.38500000D-02	0.00000000D+00	LE	1	
9	0.00000000D+00	1.00100000D-01	0.00000000D+00	LE	1	
10	0.00000000D+00	1.16350000D-01	0.00000000D+00	LE	1	

Figure 3.12: Nodes.DAT file

In the connectivity and nodes files, particularly for the beam approach, we observe that the expansion occurs in the third direction, which is handled using the Finite Element Method (FEM). In the beam approach, this third direction is consistently the y-axis. In the 'nodes.dat' file, the first column represents the node ID, while the subsequent three columns correspond to the x, y, and z coordinates of each node. The term "LE" stands for the Lagrange model used in the analysis. In the 'CONNECTIVITY.dat' file, the finite elements of the structure are defined, and for each element, the associated nodes are specified. These nodes are listed in a specific order, according to a local numbering system that depends on the type of element being used. Importantly, the list of element nodes is expressed in terms of global numbering, which references the overall node identification within the entire structure.

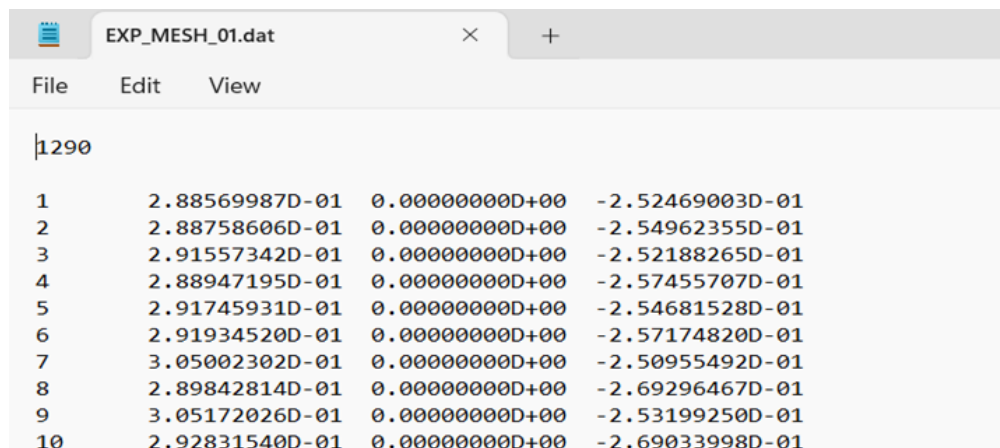


File	Edit	View			
36	0.0D0	0.0D0			
B2	1	1	2	1	3
B2	2	2	3	1	1
B2	3	3	4	1	2
B2	4	4	5	1	2
B2	5	5	6	1	2
B2	6	6	7	1	2
B2	7	7	8	1	2
B2	8	8	9	1	2
B2	9	9	10	1	2
B2	10	10	11	1	2
B2	11	11	12	1	2

Figure 3.13: Connectivity.DAT file

In the figure 3.13, the first column indicates the element type. In our case, it is labelled as B2, which denotes linear elements that connect two nodes. The second column represents the element ID, while the third and fourth columns specify the nodes associated with the element. The fifth column provides the versor, and the sixth column details the 'exp_mesh' and 'exp_connectivity' parameters.

EXP_MESH_0X.dat: This file contains the enumerated list of expansion nodes. Each node in this list is assigned a unique number according to a global numbering rule. The global list of these expansion nodes is specifically defined along the x and z directions, ensuring that the nodes are correctly positioned and referenced within the overall structure.



File	Edit	View			
1290					
1	2.88569987D-01	0.00000000D+00	-2.52469003D-01		
2	2.88758606D-01	0.00000000D+00	-2.54962355D-01		
3	2.91557342D-01	0.00000000D+00	-2.52188265D-01		
4	2.88947195D-01	0.00000000D+00	-2.57455707D-01		
5	2.91745931D-01	0.00000000D+00	-2.54681528D-01		
6	2.91934520D-01	0.00000000D+00	-2.57174820D-01		
7	3.05002302D-01	0.00000000D+00	-2.50955492D-01		
8	2.89842814D-01	0.00000000D+00	-2.69296467D-01		
9	3.05172026D-01	0.00000000D+00	-2.53199250D-01		
10	2.92831540D-01	0.00000000D+00	-2.69033998D-01		

Figure 3.14: Exp_mesh.DAT file.

EXP_CONN_0X.dat: This file defines the expansion elements and specifies the

associated nodes for each element. The nodes of each element are listed in an ordered sequence, following a local numbering system that depends on the type of element. The list of nodes for each element is expressed using global numbering, ensuring consistency across the entire structure.

Element	1	2	3	4	5	6	7
Q4	1	1	1285	1287	1284	1283	
Q4	2	1	1283	1284	1279	1278	
Q4	3	1	1278	1279	1276	1273	
Q4	4	1	1273	1276	1271	1269	
Q4	5	1	1269	1271	1264	1262	
Q4	6	1	1262	1264	1259	1254	
Q4	7	1	1287	1285	1286	1289	
Q4	8	1	1289	1286	1288	1290	
Q4	9	1	1254	1259	1253	1251	
Q4	10	1	1251	1253	1248	1244	
Q4	11	1	1244	1248	1242	1239	
Q4	12	1	1239	1242	1237	1232	

Figure 3.15: Exp_CONN.DAT file.

In the file 'MATERIAL.dat', the number of materials used in the analysis and their mechanical properties are defined and initialized within the code. For isotropic materials, designated as 'ISO-M', only three parameters need to be specified: the Young's modulus (E), Poisson's ratio (ν), and material density as shown in the Figure3.16

Material	1	2	3	4	5
ISO-M	1	70.009	0.3300	2700.000	
ISO-M	2	99.0015	0.28600	0.000100	

Figure 3.16: ISO-M Material.DAT file.

For orthotropic materials, designated as ORT-M, a more comprehensive set of parameters is required. This includes the Young's moduli along different axes, shear moduli, and all relevant Poisson's ratios as specified on the screen Figure 3.17

```

MATERIAL.dat
File Edit View

2 2 N_MAT = total number of materials

ORT-M 1 7.00D11 7.00D11 5.19D10 0.10 0.13 0.13 5.0D10 2.29D10 2.29D10 1600.000
ISO-M 2 99.0D15 0.286D0 0.0001D0
    
```

Figure 3.17: Ort-M.DAT file.

The results, requested in the input “POSTPROCESSING.dat” are printed at the end of the analysis in the folder /STATIC (for 101, 111, ... analysis) and /DYNAMIC (for 103, 106, ... analysis) of the main code folder Figure 3.9.

```

C:\Users\DEEPAK NC\OneDrive x + v
+-----+
|      00      00      0000      |
| 0000 0000 00 00 00 0000000    |
| 00 0000 00 00 00 00 0 00      |
| 00 00 00 00 00 00 00          |
| 00 00 00 0000000 00000 00 00   |
| 00 00 00000 00000 0000000     |
| 00 00000000                    |
|      NODE DEPENDENT KINEMATICS CODE      |
|      VERSION 1.06 (Magliacano) - release 01/12/2023      |
|      Politecnico di Torino                    |
+-----+

INPUT DIR   : C:\Users\DEEPAK NC\OneDrive\Desktop\MUL code\CUF_20240131_101
RUN STARTED AT : 14 August 2024 10:31:52.133 PM

--> INPUT FILES READING:      OK
--> INPUT DATA PROCESSING:   OK
--> MATERIAL PROPERTIES EVALUATION:OK
--> PROCEDURE 101 - MECHANICAL STATIC ANALYSIS:
Classical Model=1 , Tow Angle Model=2
Insert the option=
1
--> K UU MATRIX EVALUATION:      Beam FNs No MITC
OK
--> DOF :      54450
--> K_NZ:      3057858 ( 0.10% FULL)
--> MATRIX ALLOCATION:           OK
--> BC APPLICATION:             OK
--> F_BF_VECTOR EVALUATION:     OK
--> SOLUTION COMPUTATION:       OK
--> POSTPROCESSING:             Performing 1D postprocessing - PARA
    
```

Figure 3.18: MUL2

3.3 Modal analysis of Central Wing Box

3.3.1 Analysis overview

Modal analysis is a critical aspect of structural engineering and dynamics, focusing on understanding and characterizing the vibrational behaviour of structures and components. This analytical technique identifies the natural frequencies and mode shapes of a system, which are essential for predicting how structures respond to various dynamic loads. The importance of modal analysis lies in its ability to ensure the safety, reliability, and performance of structures by preventing resonance, which can lead to catastrophic failures. Resonance occurs when the frequency of external forces matches a structure's natural frequency, leading to large amplitude oscillations. This foundational knowledge allows for better prediction and mitigation of dynamic responses, ensuring structural integrity and performance throughout the lifecycle of the component or structure. The significance of modal analysis extends to various fields, aerospace, automotive, civil engineering, and mechanical systems. By performing modal analysis, engineers can design structures that avoid resonant conditions, enhance durability, and optimize performance. It is particularly important in the design of aircraft, and machinery, where dynamic loads such as wind, and operational vibrations are prevalent. Understanding the modal characteristics helps in improving noise and vibration performance, leading to quieter and more comfortable products.

The central wing box is a critical structural component in an aircraft, acting as the main load-bearing element connecting the wings to the fuselage. Understanding its dynamic behaviour is essential for ensuring structural integrity and performance under various operational conditions. Free vibration analysis involves studying the natural oscillation of a structure when it is disturbed from its equilibrium position and then allowed to vibrate without external forces acting on it. The main parameters of interest in free vibration analysis are the natural frequencies (eigenfrequencies) and mode shapes (eigenmodes). These parameters help identify the dynamic characteristics of the structure and are vital for designing components that can withstand dynamic loads and avoid resonance. For the initial analysis, aluminium is chosen as the material for the central wing box due to its isotropic properties. Isotropic materials have uniform mechanical properties in all directions, simplifying the analysis and focusing on the fundamental vibration characteristics. Aluminium is widely used in aerospace applications because of its high strength-to-weight ratio, good corrosion resistance, and ease of fabrication. While conducting modal analysis for my thesis, I chose to use the Carrera Unified Formulation (CUF) instead of Abaqus. The primary reason for this decision was the nature of the modes obtained from each method. In Abaqus, the computed modes often tend to

be localized, meaning that the vibration patterns are confined to specific regions of the structure. These localized modes do not provide a clear understanding of the overall dynamic behaviour of the structure, as they may overlook important global deformation patterns. As a result, the analysis may miss critical insights into the structural dynamics that are essential for accurate evaluation and optimization. In contrast, the Carrera Unified Formulation offers a more refined approach to modal analysis. CUF provides a higher level of accuracy in capturing the global modes of the structure. By leveraging advanced mathematical techniques, CUF ensures that the modal shapes are well-defined and representative of the entire structure's dynamic behaviour. This comprehensive representation allows for a more accurate assessment of the structural performance under dynamic loading conditions. Therefore, to achieve more reliable and insightful results in my modal analysis, I utilized the Carrera Unified Formulation instead of Abaqus. This choice ensured that the obtained modes accurately reflected the global behaviour of the structure, providing a better foundation for subsequent analyses and design decisions.

Mode shape	Frequency (Hz)
Frequency 1:	449.78
Frequency 2:	510.14
Frequency 3:	573.11
Frequency 4:	620.48
Frequency 5:	663.45
Frequency 6:	718.81
Frequency 7:	742.54
Frequency 8:	749.33
Frequency 9:	753.22
Frequency 10:	771.26
Frequency 11:	776.87
Frequency 12:	800.57
Frequency 13:	823.56
Frequency 14:	865.32
Frequency 15:	883.21
Frequency 16:	897.37
Frequency 17:	948.79
Frequency 18:	993.32
Frequency 19:	996.83
Frequency 20:	1064.81

Table 3.1: Frequency Table.

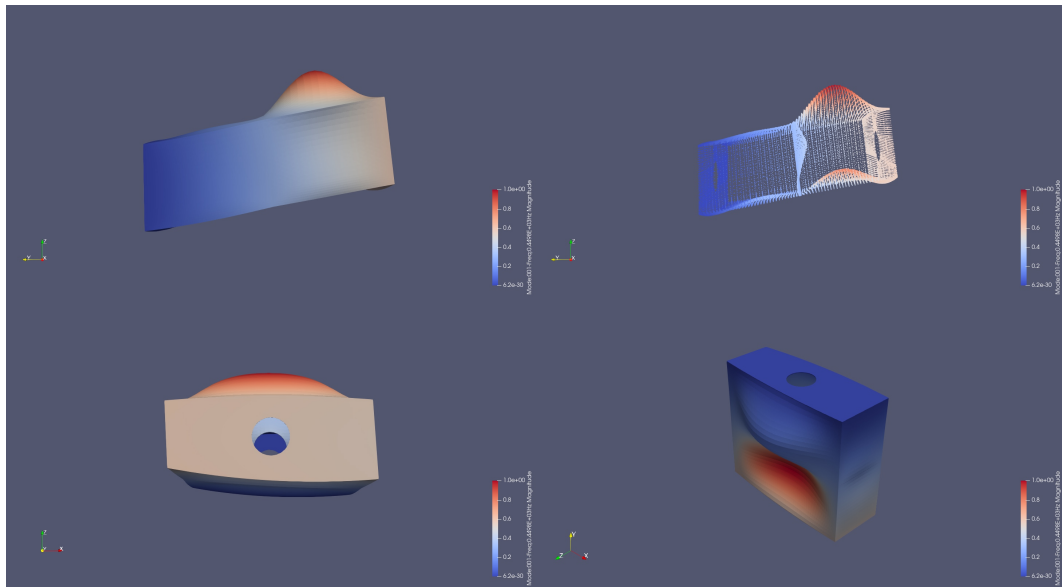


Figure 3.19: Mode Shape 1.

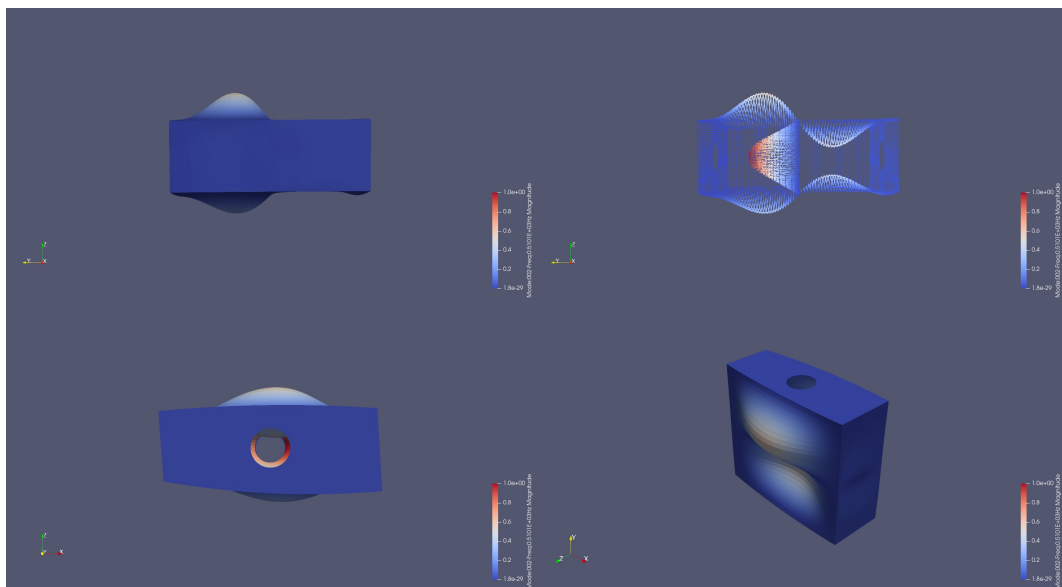


Figure 3.20: Mode Shape 2.

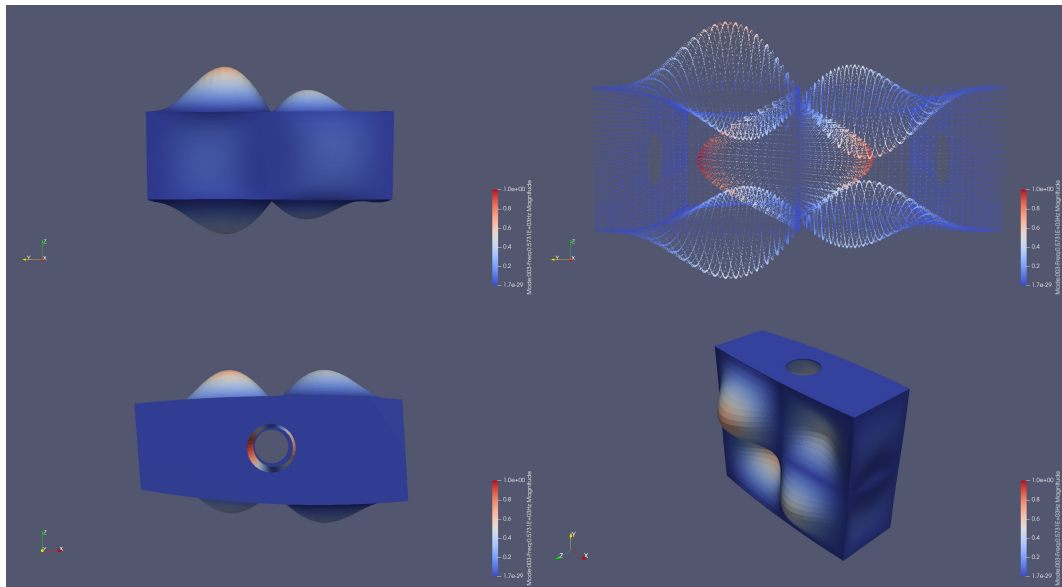


Figure 3.21: Mode Shape 3.

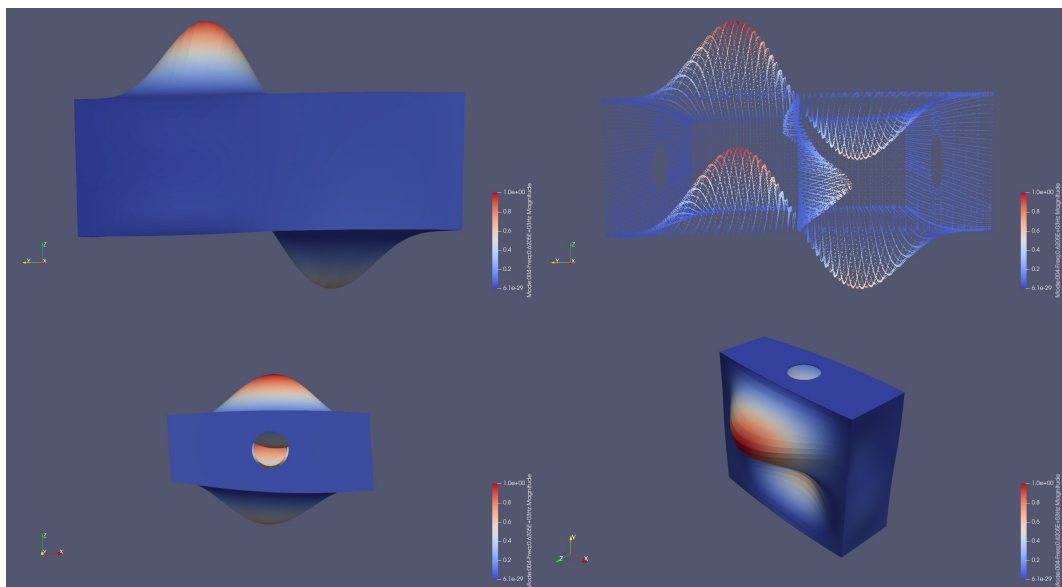


Figure 3.22: Mode Shape 4.

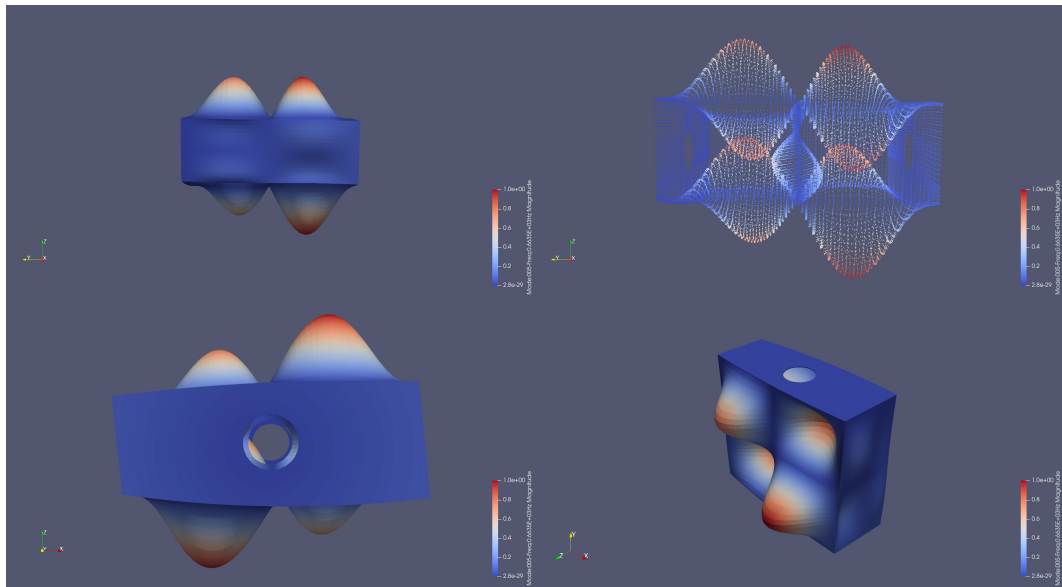


Figure 3.23: Mode Shape 5.

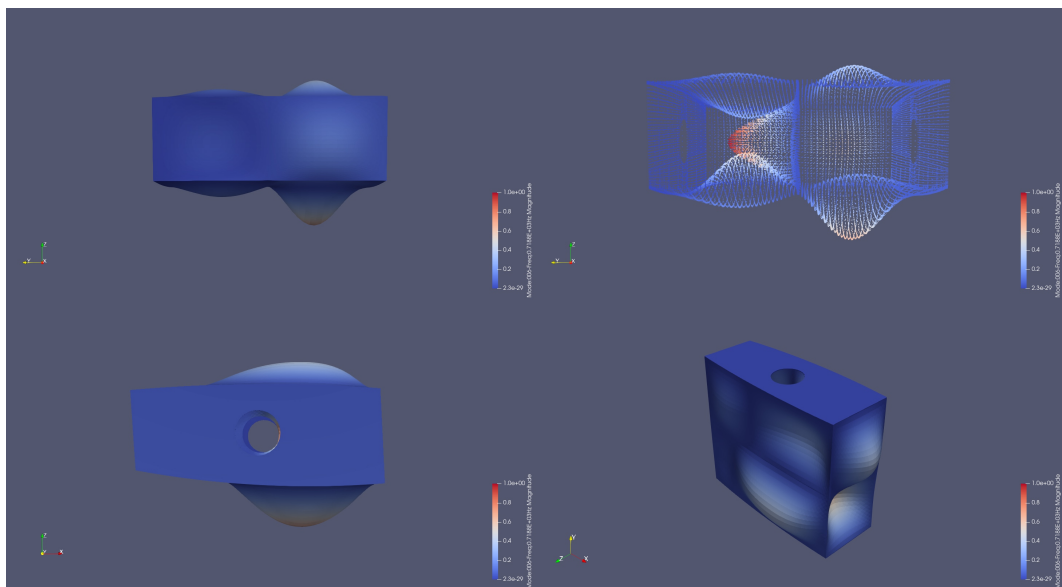


Figure 3.24: Mode Shape 6.

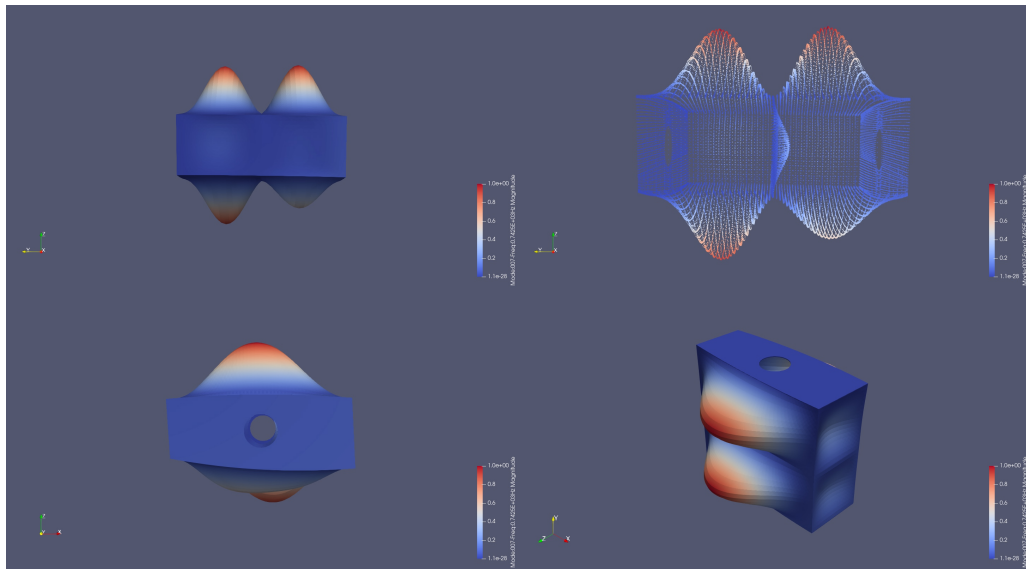


Figure 3.25: Mode Shape 7.

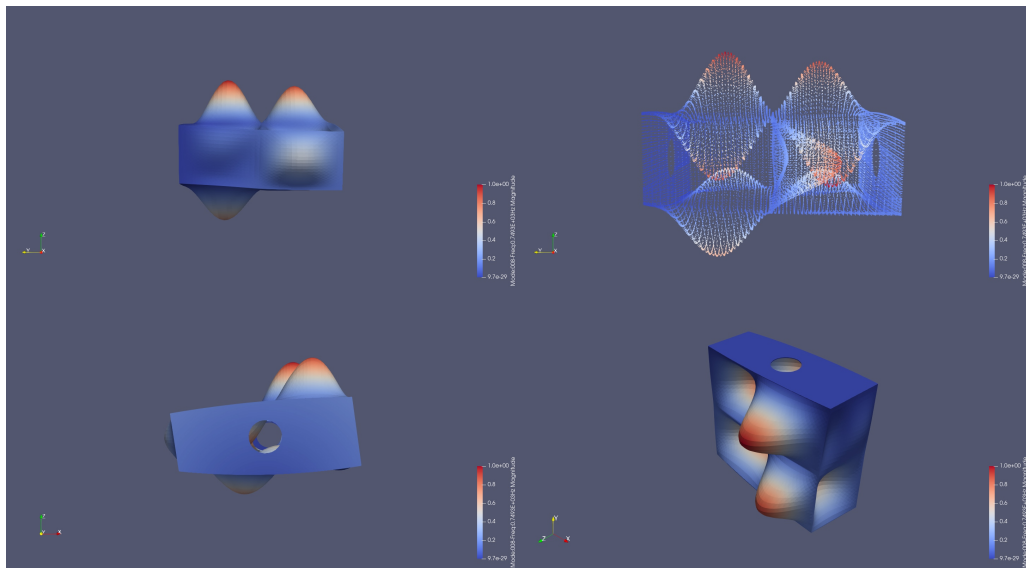


Figure 3.26: Mode Shape 8.

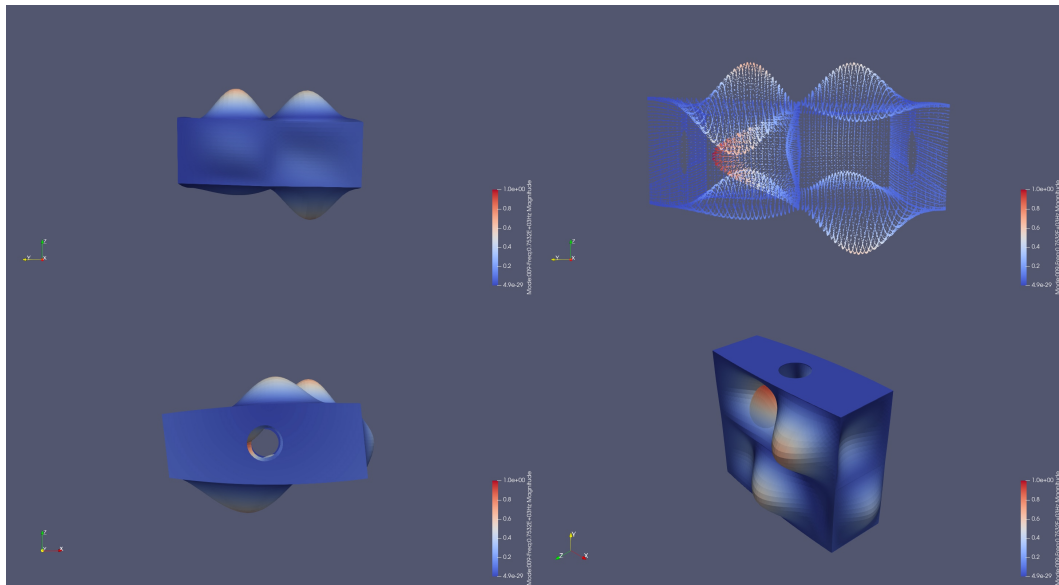


Figure 3.27: Mode Shape 9.

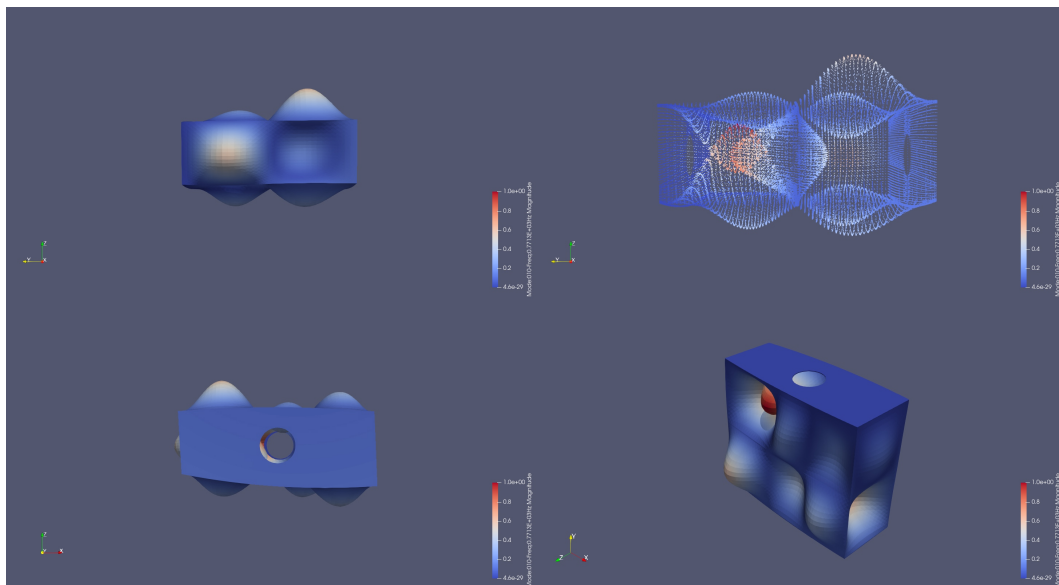


Figure 3.28: Mode Shape 10.

3.3.2 Conclusion

The mode shape corresponding to a frequency, indicates the specific pattern of deformation that the central wing box undergoes at this particular natural frequency.

This mode shape is characterized by

Deformation Pattern: The visualization of the mode shape shows that certain areas of the wing box experience larger displacements compared to others.

Nodal Points/ lines: Points or lines where maximum displacement and no movement occurs (nodes) are observed. These are critical as they define regions of zero displacement amidst vibrating areas. During the modal analysis of the central wing box, it was observed that the maximum displacement occurs in three key areas:

Displacement at the skin The skin acts as the primary surface exposed to aerodynamic forces and plays a crucial role in maintaining the aerodynamic shape and overall structural integrity of the wing box. The deformation observed in the skin suggests a bending mode, where the outer surfaces are more flexible and relatively lower stiffness compared to the internal structure. This bending leads to significant displacements on the skin. The maximum displacement typically occurs in areas furthest from support points, such as the mid-span sections between ribs. This behaviour aligns with the principles of beam bending, where the maximum deflection is observed at the centre of the span for a simply supported beam.

Displacement at the centre rib structure The ribs provide the necessary support and distribute the load from the skin to the rest of the wing box structure. The centre rib, in particular, is crucial for maintaining the overall shape and stiffness. The centre rib might show maximum displacement in response to torsional modes or combined bending-torsion modes due to its role in providing lateral support and transferring loads between upper and lower skins.

Spar deformation The spars, acting as the primary load-bearing components, experience displacements influenced by both bending and torsional loads. displacement in the spars is generally at the mid span, depending on the mode. Spars can be analysed using beam theory. The deformation pattern often exhibits a combination of flexural and torsional modes, especially at higher frequencies.

In modal analysis of a wing box, understanding the maximum displacement in the skin, centre rib structure, and spars is critical for predicting the dynamic behaviour and ensuring the structural and operational integrity of the wing. By describing the deformation patterns in terms of structural mechanics, engineers can better assess the potential implications and take appropriate measures to enhance the durability and performance of the wing box.

3.4 Static Analysis of Central Wing Box

3.4.1 Analysis Overview

In this study, I performed a comprehensive static analysis to assess the structural integrity and performance of a central wing box under expected load conditions,

excluding dynamic effects such as vibration or impact. Using two different modelling approaches—solid and shell models—I analysed the displacements to ensure they remained within safe limits, as excessive deformations can alter the aerodynamic profile of the wing, leading to reduced efficiency and performance. Identifying potential failure points is crucial to reinforce these areas and prevent catastrophic failure during operation. The analysis was conducted using isotropic aluminium, characterized by uniform properties in all directions, and an equivalent orthotropic material, which has direction-dependent properties to mimic composite materials. Simulations were executed in Abaqus, a sophisticated finite element analysis (FEA) software that supports complex material models and nonlinear behaviour. To further validate the results obtained for the solid model in Abaqus, I employed the Carrera Unified Formulation (CUF). CUF is preferred over traditional FEA methods due to its higher-order formulation capabilities, which provide more accurate and efficient modelling of complex structures and anisotropic materials. The higher-order terms in CUF capture detailed stress distributions and deformation behaviours with fewer computational resources, ensuring robust analysis for both isotropic and orthotropic materials. This dual-approach analysis helps ensure the structural integrity and reliability of the wing box, thereby enhancing the safety and performance of the aircraft.

Material and Material ID	Solid model Deformation	CUF Model Deformation	Shel Deformation
Aluminium	3.50E-03	3.40E-03	3.13E-03
1	6.80E-04	8.10E-04	6.02E-04
2	1.33E-03	1.40E-03	1.18E-03
3	1.19E-03	1.80E-03	9.65E-04
4	4.82E-04	5.00E-04	4.60E-04
5	4.40E-04	5.60E-04	4.34E-04
6	3.93E-04	3.90E-04	3.87E-04
7	9.36E-04	9.30E-04	8.80E-04
8	1.00E-03	9.60E-04	1.06E-03
9	4.20E-04	3.40E-04	4.20E-04

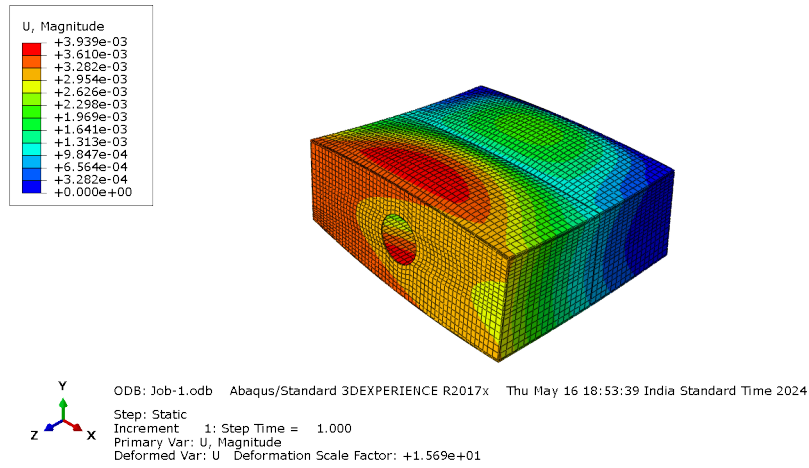


Figure 3.29: Aluminium solid deformation Using Classical FEM.

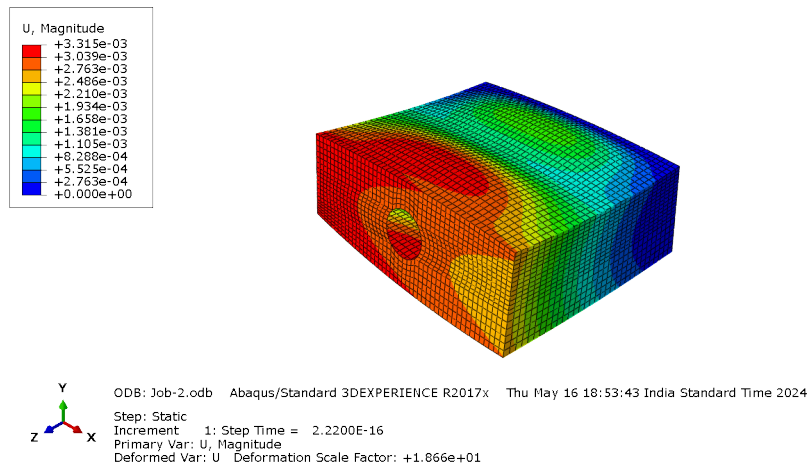


Figure 3.30: Aluminium shell deformation using Classical FEM.

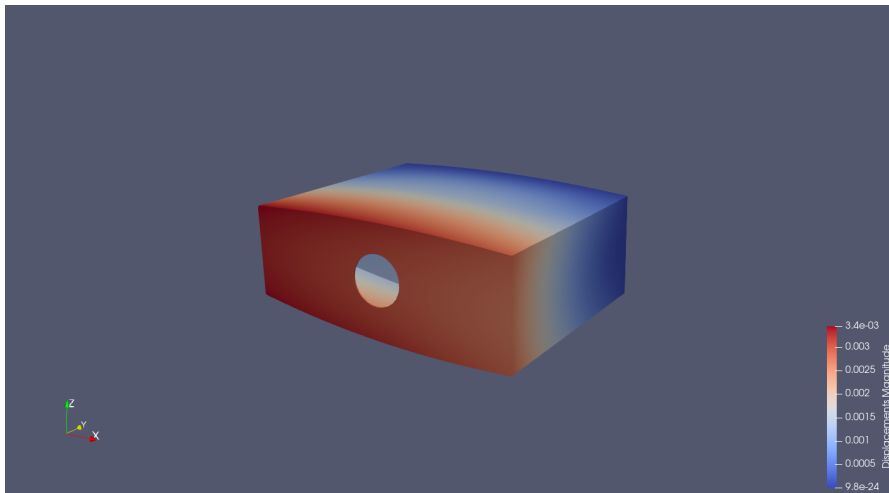


Figure 3.31: Aluminium deformation Using CUF.

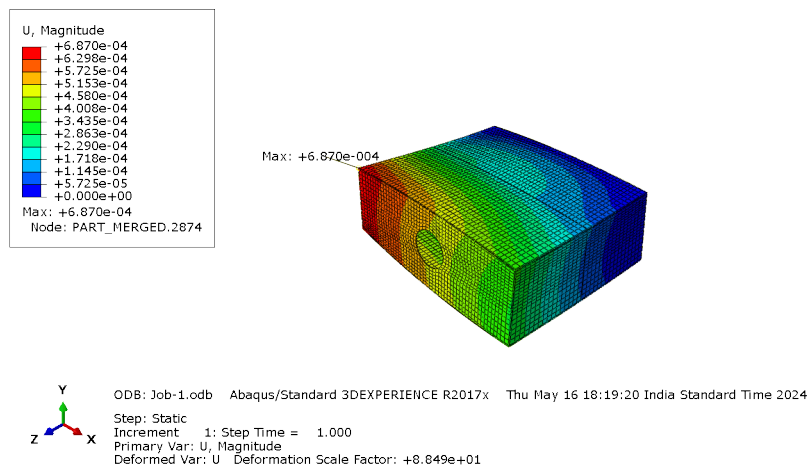


Figure 3.32: STD CF Fabric solid deformation using Classical FEM.

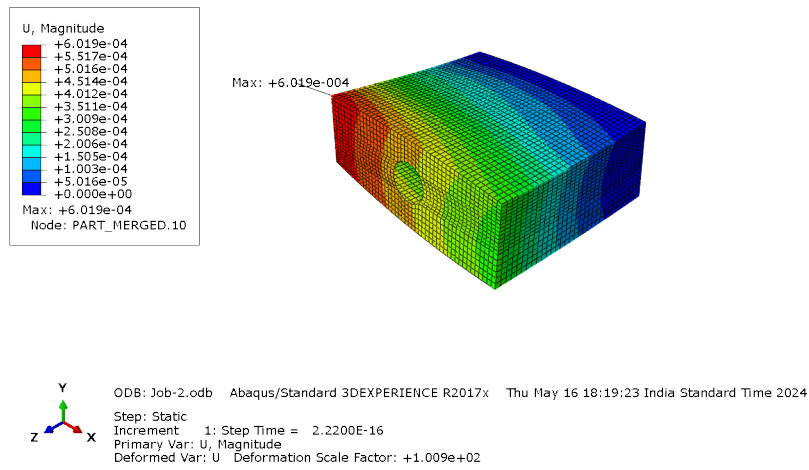


Figure 3.33: STD CF Fabric Shell deformation using Classical FEM.

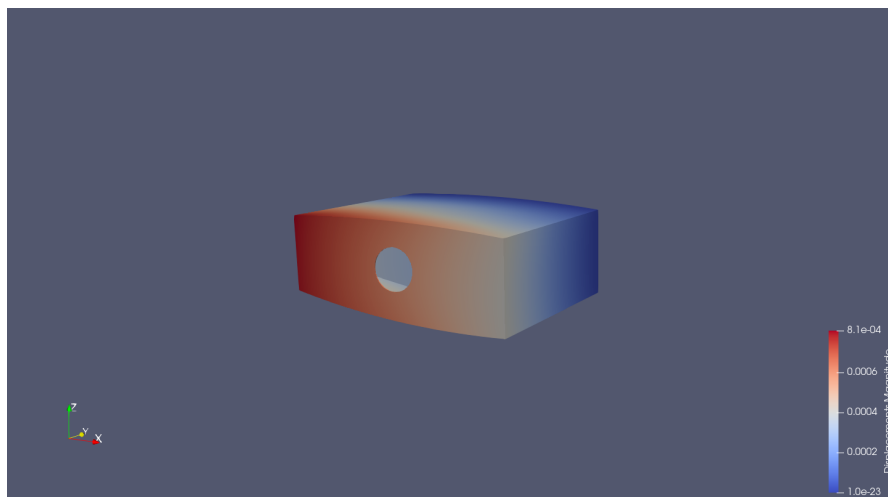


Figure 3.34: STD CF Fabric deformation using CUF.

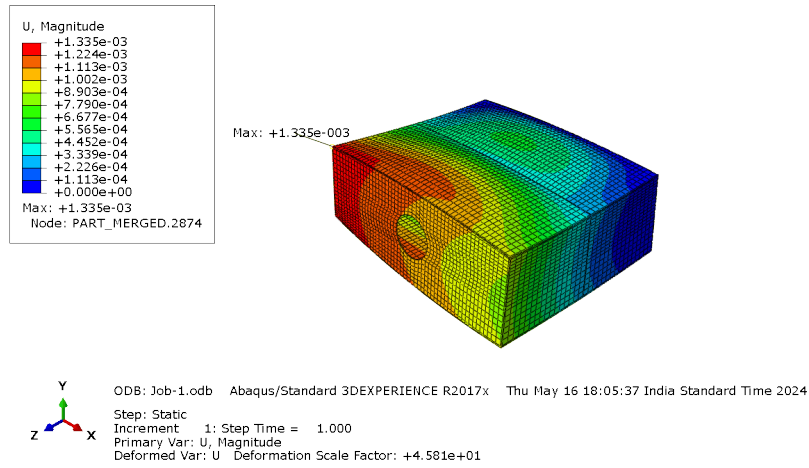


Figure 3.35: E Glass Fabric solid deformation using Classical FEM.

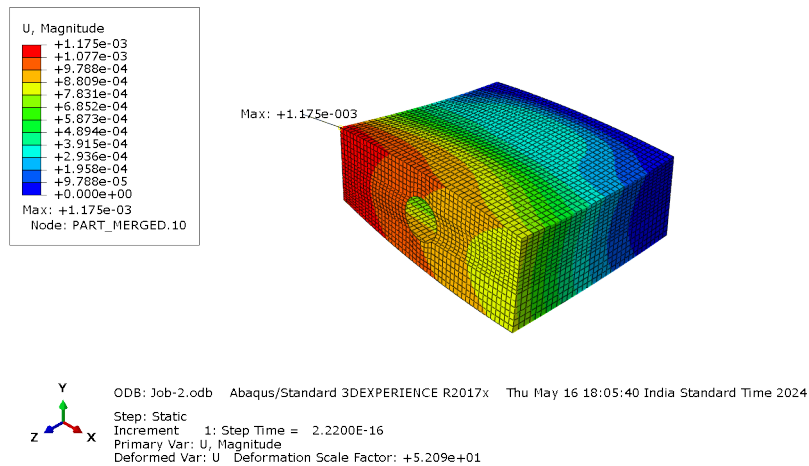


Figure 3.36: E Glass Fabric Shell deformation using Classical FEM.

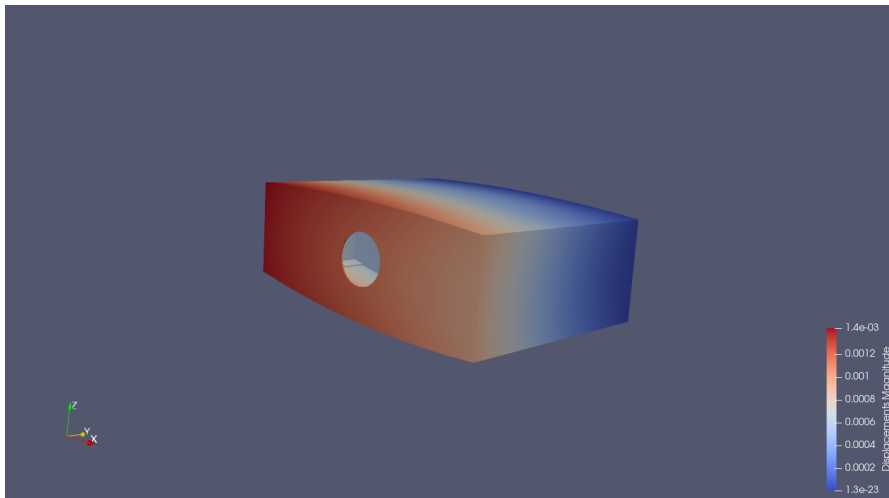


Figure 3.37: E Glass Fabric deformation using CUF.

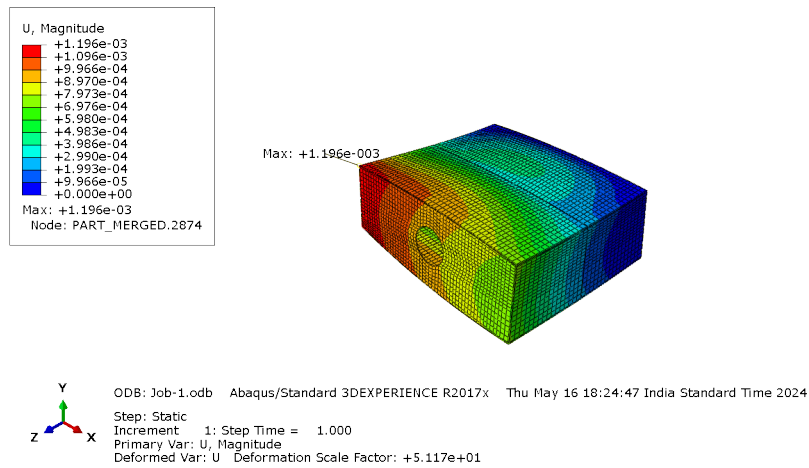


Figure 3.38: Kevlar Fabric solid deformation using Classical FEM.

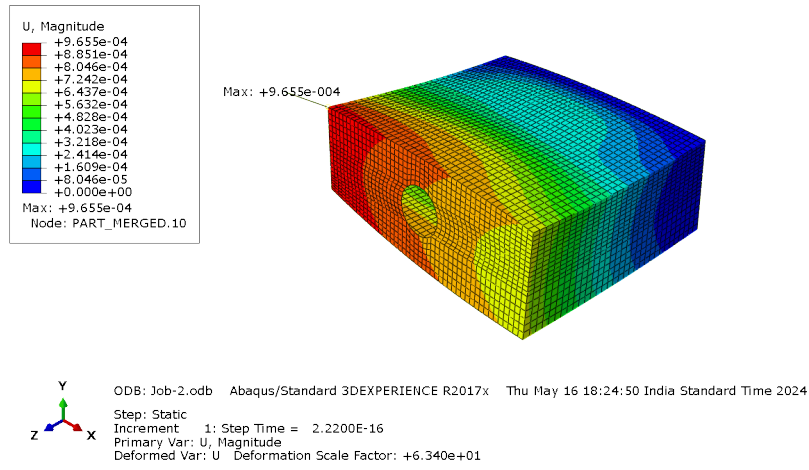


Figure 3.39: Kevlar Fabric shell deformation using Classical FEM.

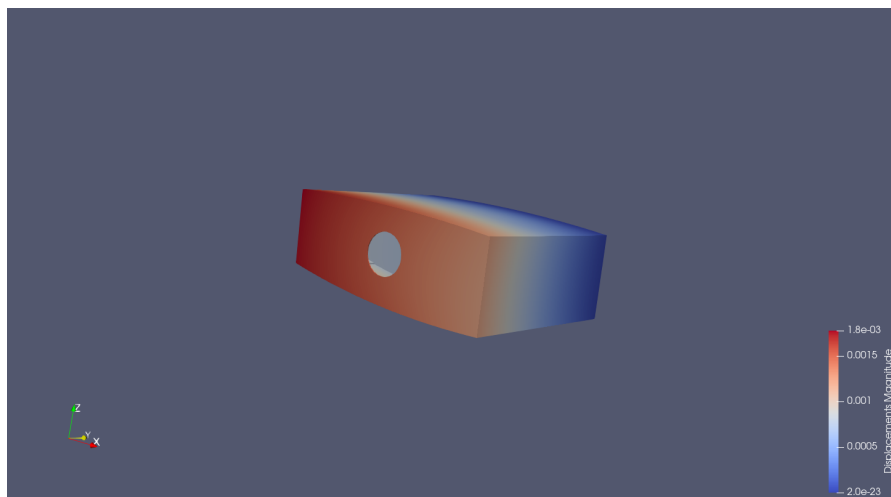


Figure 3.40: Kevlar Fabric deformation using CUF.

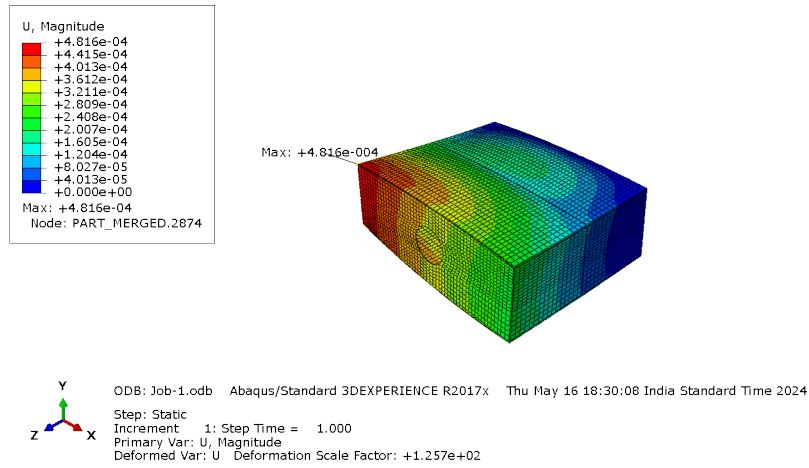


Figure 3.41: STD CF UD solid deformation using Classical FEM.

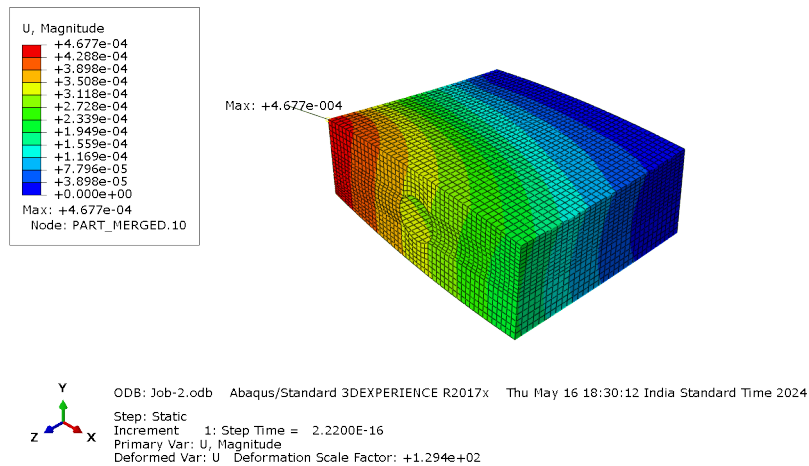


Figure 3.42: STD CF UD shell deformation using Classical FEM.

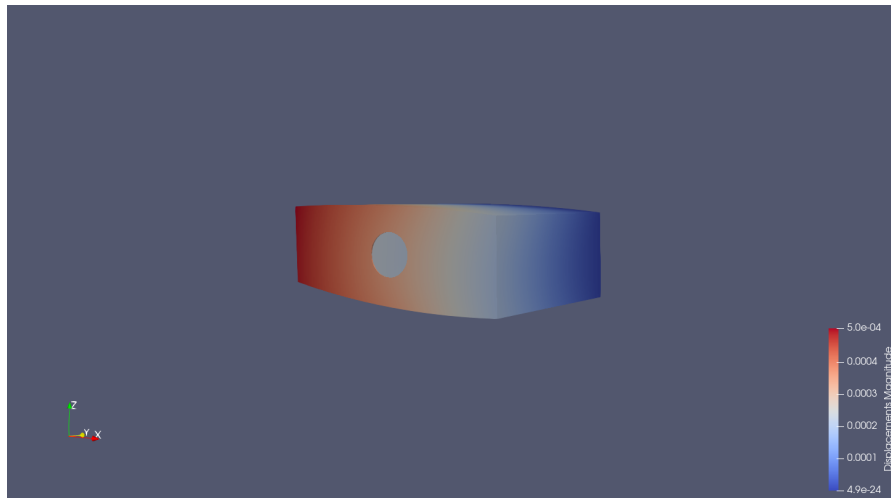


Figure 3.43: STD CF UD deformation using CUF.

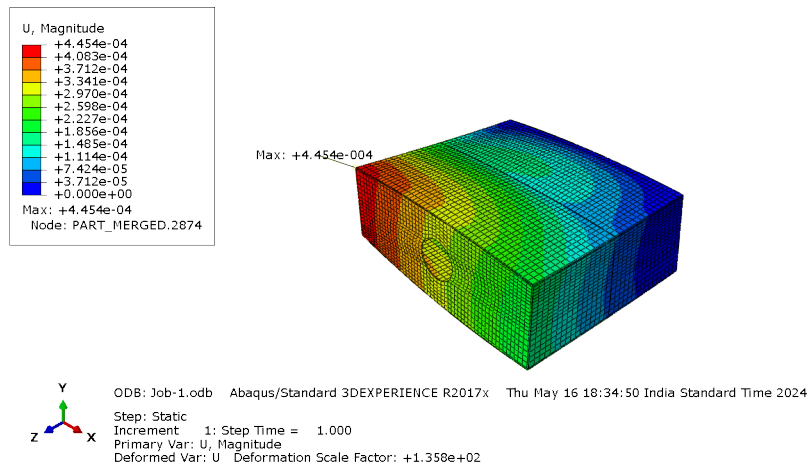


Figure 3.44: HMCF UD solid deformation using Classical FEM.

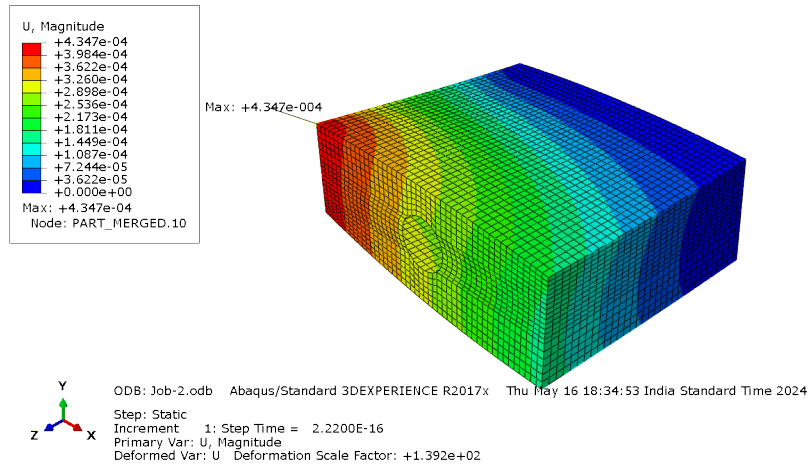


Figure 3.45: HMCF UD Shell deformation using Classical FEM.

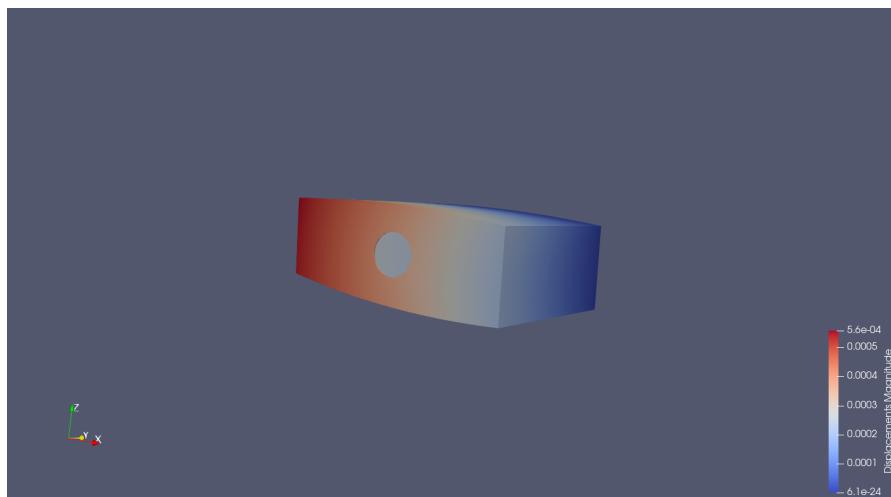


Figure 3.46: HMCF UD deformation using CUF.

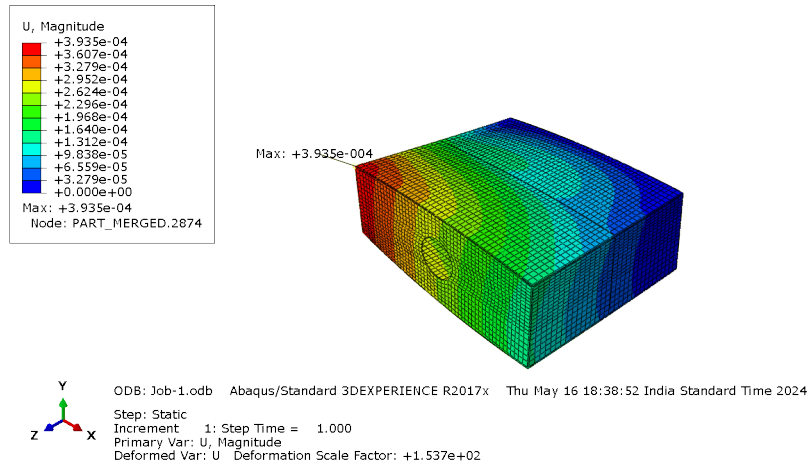


Figure 3.47: M55 UD solid deformation using Classical FEM

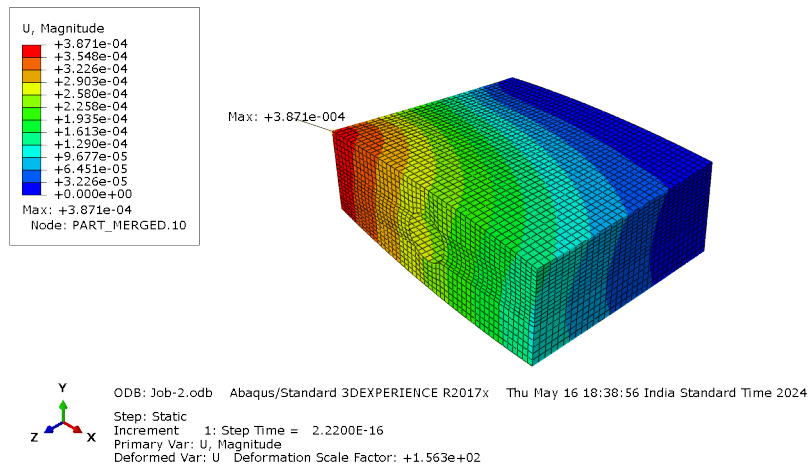


Figure 3.48: M55 UD shell deformation using Classical FEM.

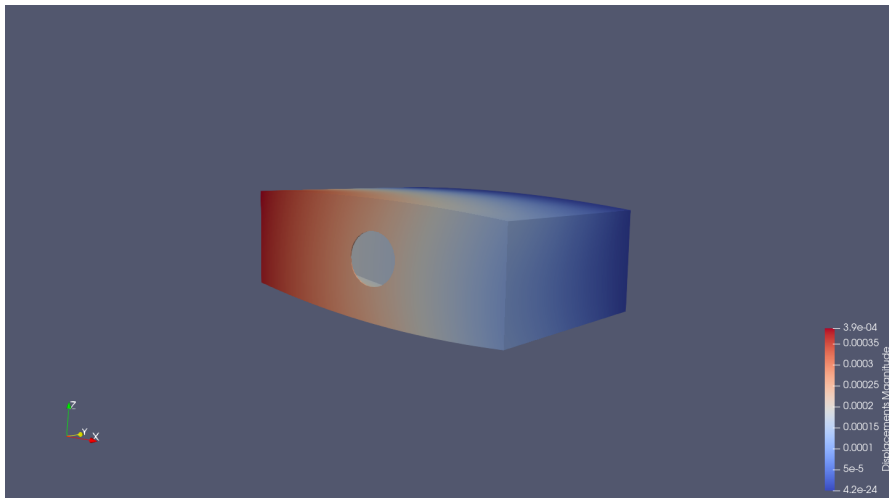


Figure 3.49: M55 UD deformation using CUF.

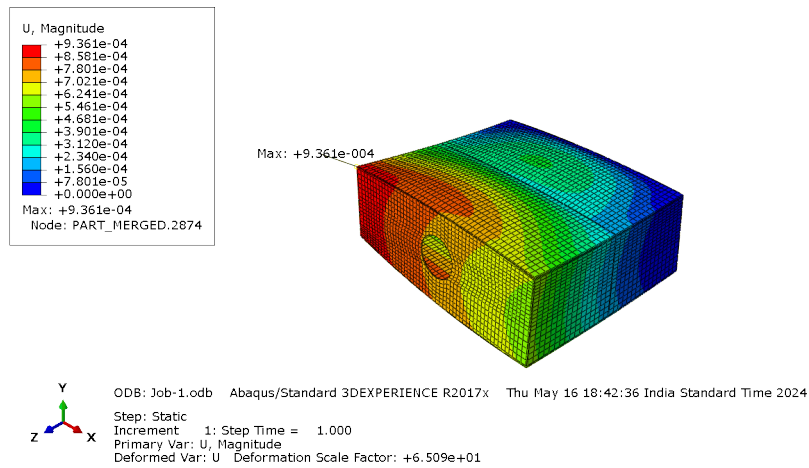


Figure 3.50: E Glass UD solid deformation using Classical FEM.

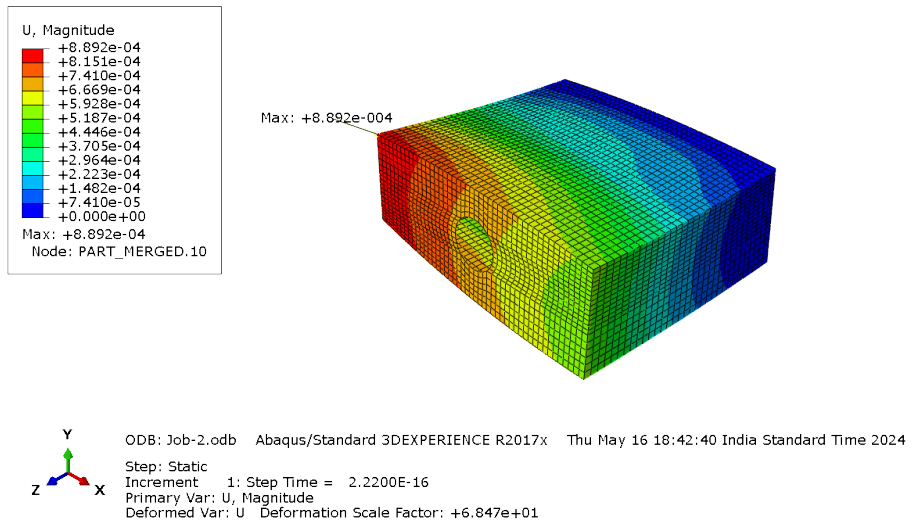


Figure 3.51: E Glass UD Shell deformation using Classical FEM.

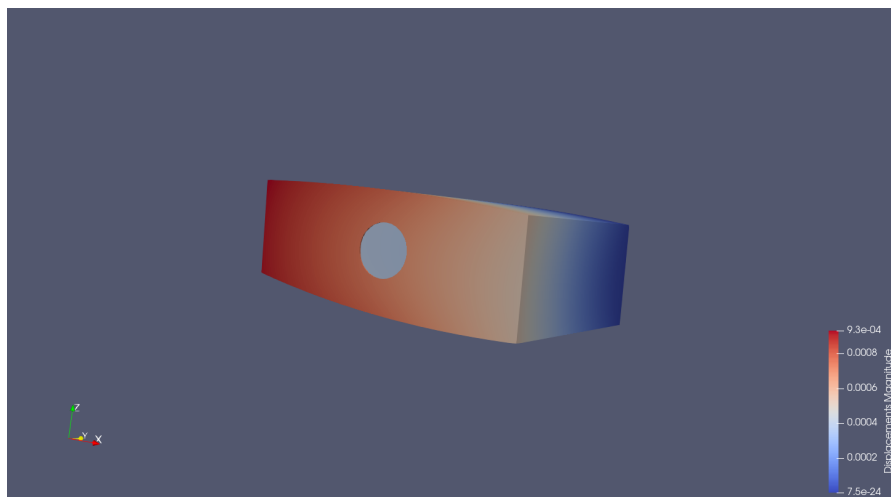


Figure 3.52: E Glass UD deformation using CUF.

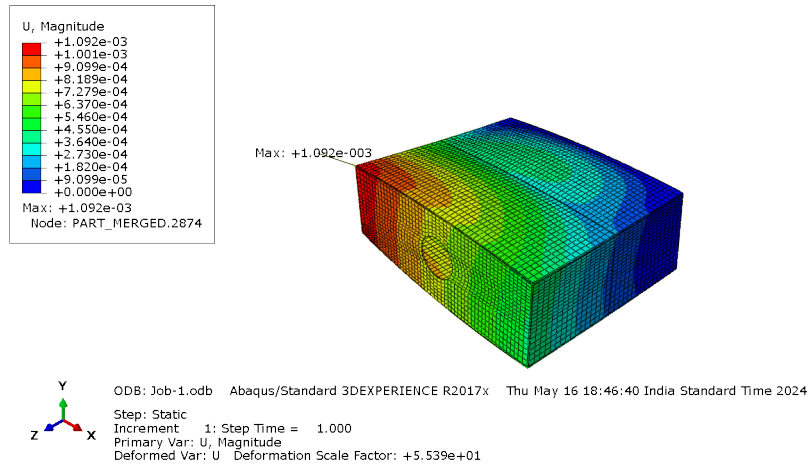


Figure 3.53: Kevlar UD solid deformation using Classical FEM.

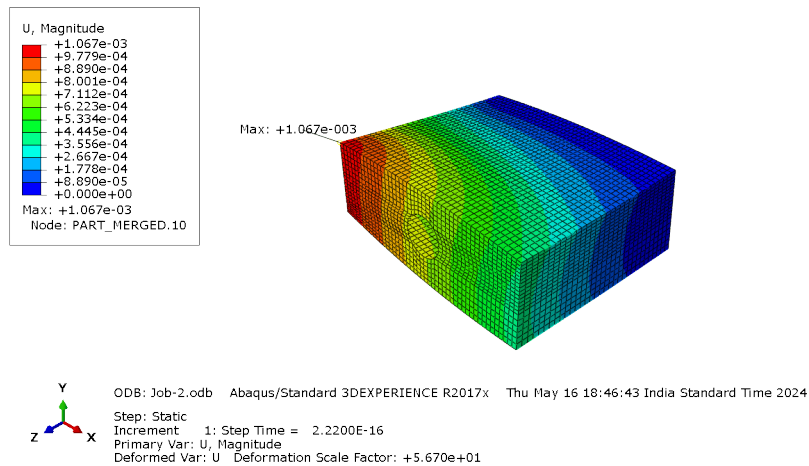


Figure 3.54: Kevlar UD Shell deformation using Classical FEM.

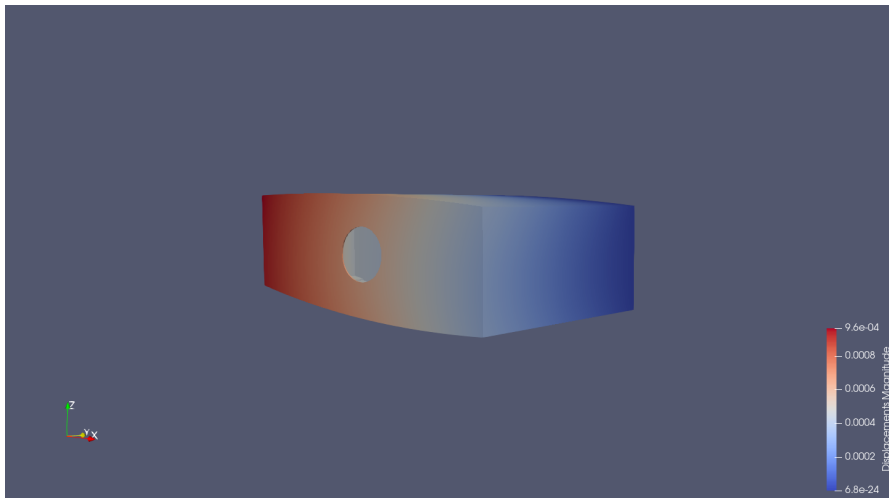


Figure 3.55: Kevlar UD Deformation Using CFU.

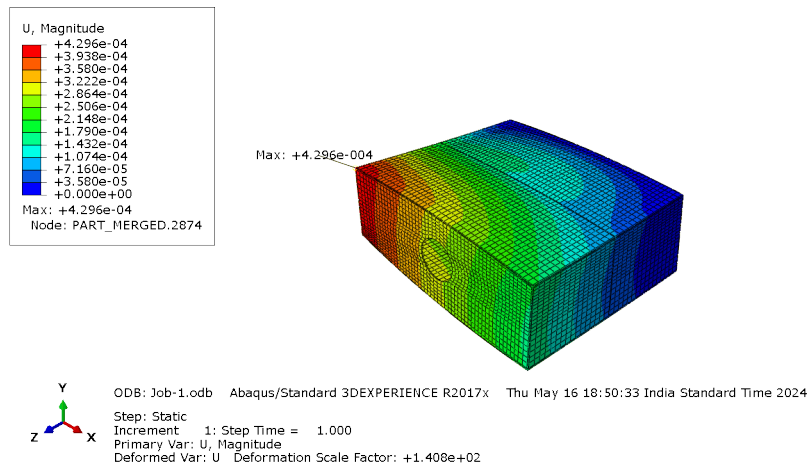


Figure 3.56: Boron UD solid deformation using Classical FEM.

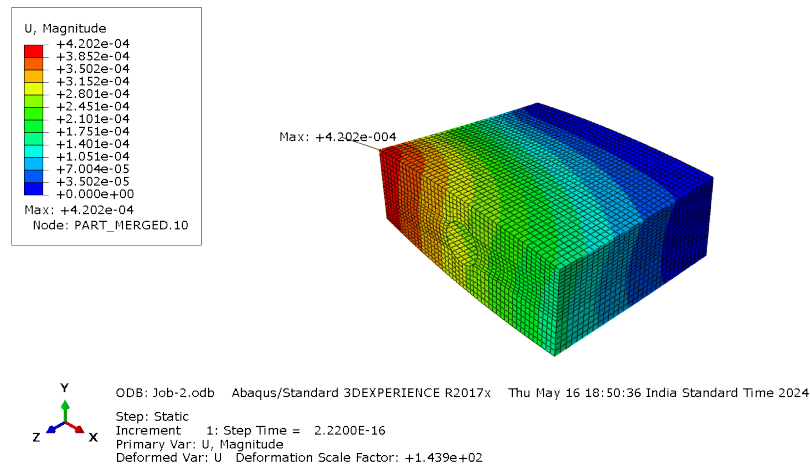


Figure 3.57: Boron UD Shell deformation using Classical FEM.

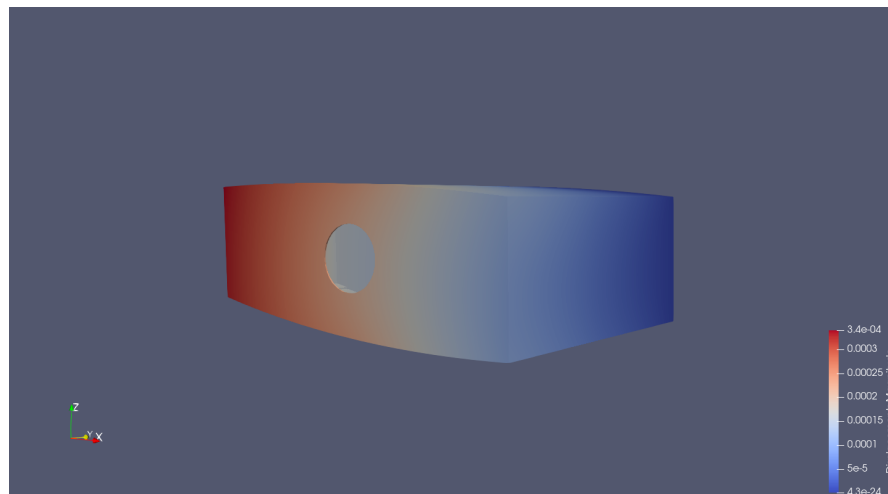


Figure 3.58: Boron UD deformation using CUF .

3.4.2 Conclusion

The deformation results across various materials and modelling approaches highlight the robustness of both Abaqus and the Carrera Unified Formulation (CUF) in predicting the structural behaviour of the central wing box. The deformation values obtained from both the solid model in Abaqus and the CUF model are remarkably similar, underscoring the accuracy and reliability of these methods. This consistency in deformation predictions across different models and materials demonstrates the effectiveness of Abaqus and CUF in structural analysis and their capability to produce precise and dependable results.

The shell model results consistently showed slightly lower deformations compared to the solid models, which is expected due to the reduced dimensionality and associated assumptions in shell modeling. This reinforces the importance of selecting the appropriate modeling approach based on the specific requirements of accuracy and computational efficiency.

Additionally, the figure in the results shows a model with one end constrained and the other end free, leading to greater deformation at the free end. Technically, this observation aligns with the concept that stress is maximized at the constrained end due to the fixed boundary condition.

3.5 Failure Analysis For The Composite Materials

3.5.1 Analysis Overview

The Tresca and von Mises criteria are commonly used to predict yielding in isotropic, ductile materials such as metals. However, when dealing with composite materials, these criteria are generally not appropriate due to the anisotropic nature of composites, which have different properties in different directions. Composite materials, particularly Fiber-reinforced composites, exhibit complex failure mechanisms due to their heterogeneous nature. For such materials, more specialized criteria are used

- Maximum Stress Criterion.
- Tsai-Wu Criterion.
- Tsai-Hill Criterion.

In this comprehensive study, the failure indices for seven different composite materials under six distinct stacking sequences were meticulously analysed to understand their structural performance under load and to facilitate computational efficiency, especially given the need to account for the stacking sequence of composite materials and the associated numerical limitations, I opted to use a shell model. The shell model is advantageous in this context because it significantly reduces the computational complexity compared to a solid model, making it a more suitable choice for intricate simulations. The stacking sequences evaluated were

- $90^\circ/45^\circ/ - 45^\circ/0^\circ$,
- $90^\circ/0^\circ/45^\circ/ - 45^\circ$,
- $45^\circ/ - 45^\circ/0^\circ/90^\circ$,

- $90^\circ/0^\circ/90^\circ/0^\circ$,
- $45^\circ/-45^\circ/45^\circ/-45^\circ$,
- $60^\circ/30^\circ/-30^\circ/-60^\circ$.

Material ID	Material	Density ρ [kg/m ³]
1	Std CF Fabric	1600
2	E glass Fabric	1900
3	Std CF UD	1600
4	M55 UD	1650
5	E glass UD	1900
6	Kevlar UD	1400
7	Boron UD	2000

Table 3.2: Properties and Densities of the materials used.

Material ID	Young's Modulus (Pa)		
	E1	E2	E3
1	7.00E+11	7.00E+11	5.19E+10
2	2.50E+11	2.50E+11	5.00E+10
3	1.35E+12	1.00E+11	1.00E+11
4	3.00E+12	1.20E+11	1.20E+11
5	4.00E+11	8.00E+10	8.00E+10
6	7.50E+11	6.00E+10	6.00E+10
7	2.00E+12	1.50E+11	1.50E+11

Table 3.3: Mechanical properties of materials: Young's Modulus.

Material	Stacking Sequence	von Mises (Pa)	Deformation
Std CF Fabric	$90^\circ/45^\circ/-45^\circ/0^\circ$	2.23E+08	4.30E-04
	$90^\circ/0^\circ/45^\circ/-45^\circ$	2.23E+08	4.38E-04
	$45^\circ/-45^\circ/0^\circ/90^\circ$	1.23E+08	4.30E-04
	$90^\circ/0^\circ/90^\circ/0^\circ$	1.74E+08	6.02E-04
	$45^\circ/-45^\circ/45^\circ/-45^\circ$	1.43E+08	6.60E-04
	$60^\circ/30^\circ/-30^\circ/-60^\circ$	1.31E+08	4.90E-04

Table 3.7: Stacking Sequence, von Mises stress, and Deformation for Std CF Fabric.

Material ID	Shear Modulus (Pa)		
	G12	G13	G23
1	5.00E+10	2.29E+10	2.29E+10
2	4.00E+10	1.98E+10	1.98E+10
3	5.00E+10	5.00E+10	3.60E+10
4	5.00E+10	5.00E+10	4.32E+10
5	4.00E+10	4.00E+10	3.02E+10
6	2.00E+10	2.00E+10	2.08E+10
7	5.00E+10	5.00E+10	5.77E+10

Table 3.4: Mechanical properties of materials: Shear Modulus.

Material ID	Poisson's Ratio		
	NU12	NU13	NU23
1	0.10	0.13	0.13
2	0.20	0.26	0.26
3	0.30	0.33	0.39
4	0.30	0.33	0.39
5	0.25	0.25	0.325
6	0.34	0.34	0.442
7	0.23	0.23	0.299

Table 3.5: Mechanical properties of materials: Poisson's Ratio.

Material	Stacking Sequence	von Mises (Pa)	Deformation
E glass Fabric	90°/45°/-45°/0°	2.13E+08	1.16E-03
	90°/0°/45°/-45°	2.14E+08	1.15E-03
	45°/-45°/0°/90°	1.52E+08	1.81E-03
	90°/0°/90°/0°	1.83E+08	1.17E-03
	45°/-45°/45°/-45°	1.75E+08	1.30E-03
	60°/30°/-30°/-60°	1.34E+08	1.12E-03

Table 3.8: Stacking Sequence, von Mises stress, and Deformation for E glass Fabric

Material ID	Ultimate Strength (Pa)					
	S1+	S1-	S2+	S2-	S12	S23
1	6.00E+08	5.70E+08	6.00E+08	5.70E+08	9.00E+07	4.13E+07
2	4.40E+08	4.25E+08	4.40E+08	4.25E+08	7.04E+07	1.98E+07
3	1.50E+09	1.20E+09	5.00E+07	2.50E+08	7.00E+07	5.04E+07
4	1.60E+09	1.30E+09	5.00E+07	2.50E+08	7.50E+07	6.47E+07
5	1.00E+09	6.00E+08	3.00E+07	1.00E+08	4.50E+07	6.24E+07
6	1.30E+09	2.80E+08	3.00E+07	1.00E+08	4.50E+07	1.62E+07
7	1.40E+09	2.80E+09	9.00E+07	2.80E+08	1.40E+08	1.62E+08

Table 3.6: Ultimate Strength of Materials.

Material	Stacking Sequence	von Mises (Pa)	Deformation
Std CF UD	90°/45°/-45°/0°	3.67E+08	3.60E-04
	90°/0°/45°/-45°	3.65E+08	3.66E-04
	45°/-45°/0°/90°	4.46E+07	3.73E-04
	90°/0°/90°/0°	3.20E+08	5.50E-04
	45°/-45°/45°/-45°	6.40E+07	5.00E-04
	60°/30°/-30°/-60°	2.60E+08	3.40E-04

Table 3.9: Stacking Sequence, von Mises stress, and Deformation for Std CF UD.

Material	Stacking Sequence	von Mises (Pa)	Deformation
M55 UD	90°/45°/-45°/0°	3.95E+08	1.74E-04
	90°/0°/45°/-45°	3.92E+08	1.74E-04
	45°/-45°/0°/90°	3.30E+07	1.71E-04
	90°/0°/90°/0°	3.64E+08	4.27E-04
	45°/-45°/45°/-45°	4.60E+07	2.70E-04
	60°/30°/-30°/-60°	2.30E+08	2.00E-04

Table 3.10: Stacking Sequence, von Mises stress, and Deformation for M55 UD.

Material	Stacking Sequence	von Mises (Pa)	Deformation
E glass UD	90°/45°/-45°/0°	3.06E+08	1.04E-03
	90°/0°/45°/-45°	3.05E+08	1.04E-03
	45°/-45°/0°/90°	7.93E+07	1.05E-03
	90°/0°/90°/0°	2.75E+08	1.12E-03
	45°/-45°/45°/-45°	1.06E+08	1.20E-03
	60°/30°/-30°/-60°	1.76E+08	1.13E-03

Table 3.11: Stacking Sequence, von Mises stress, and Deformation for E glass UD.

Material	Stacking Sequence	von Mises (Pa)	Deformation
Kevlar UD	90°/45°/-45°/0°	3.73E+08	6.70E-04
	90°/0°/45°/-45°	3.70E+08	6.70E-04
	45°/-45°/0°/90°	3.60E+07	6.70E-04
	90°/0°/90°/0°	3.37E+08	1.22E-03
	45°/-45°/45°/-45°	5.82E+07	1.00E-03
	60°/30°/-30°/-60°	2.08E+08	7.34E-04

Table 3.12: Stacking Sequence, von Mises stress, and Deformation for Kevlar UD.

Material	Stacking Sequence	von Mises (Pa)	Deformation
Boron UD	90°/45°/-45°/0°	3.75E+08	2.50E-04
	90°/0°/45°/-45°	3.73E+08	2.52E-04
	45°/-45°/0°/90°	3.60E+07	2.51E-04
	90°/0°/90°/0°	3.42E+08	4.78E-04
	45°/-45°/45°/-45°	5.62E+07	3.73E-04
	60°/30°/-30°/-60°	2.10E+08	2.74E-04

Table 3.13: Stacking Sequence, von Mises stress, and Deformation for Boron UD.

Material	Max Stress	Tsai-Wu	Tsai-Hill
Std CF Fabric	0.38	0.17	0.18
	0.38	0.17	0.18
	0.28	0.12	0.14
	0.34	0.17	0.18
	0.57	0.38	0.39
	0.32	0.13	0.15

Table 3.14: Failure Index values for Std CF Fabric.

Material	Max Stress	Tsai-Wu	Tsai-Hill
E glass Fabric	0.51	0.48	0.49
	0.51	0.48	0.49
	1.03	1.14	1.15
	0.69	0.63	0.64
	1.59	2.62	2.63
	1.33	1.80	1.81

Table 3.15: Failure Index values for E glass Fabric.

Material	Max Stress	Tsai-Wu	Tsai-Hill
Std CF UD	0.24	0.08	0.08
	0.24	0.09	0.08
	0.04	0.39	0.21
	0.34	0.24	0.19
	0.53	0.16	0.42
	0.33	0.27	0.18

Table 3.16: Failure Index values for Std CF UD.

Material	Max Stress	Tsai-Wu	Tsai-Hill
M55 UD	0.25	0.05	0.06
	0.25	0.04	0.06
	0.23	0.20	0.06
	0.32	0.19	0.15
	0.33	0.27	0.15
	0.16	0.10	0.06

Table 3.17: Failure Index values for M55 UD.

Material	Max Stress	Tsai-Wu	Tsai-Hill
E glass UD	0.43	0.26	0.33
	0.43	0.31	0.36
	1.51	2.4	3.05
	0.6	0.6	0.63
	1.5	3.44	4.07
	1.13	1.99	2.14

Table 3.18: Failure Index values for E glass UD.

Material	Max Stress	Tsai-Wu	Tsai-Hill
Kevlar UD	0.29	0.0	0.13
	0.29	0.0	0.11
	0.73	0.61	0.57
	0.38	0.0	0.34
	0.66	0.88	0.71
	0.43	0.0	0.27

Table 3.19: Failure Index values for Kevlar UD.

Material	Max Stress	Tsai-Wu	Tsai-Hill
Boron UD	0.27	0.18	0.07
	0.27	0.18	0.07
	0.23	0.19	0.06
	0.25	0.23	0.09
	0.22	0.2	0.09
	0.15	0.17	0.05

Table 3.20: Failure Index values for Boron UD.

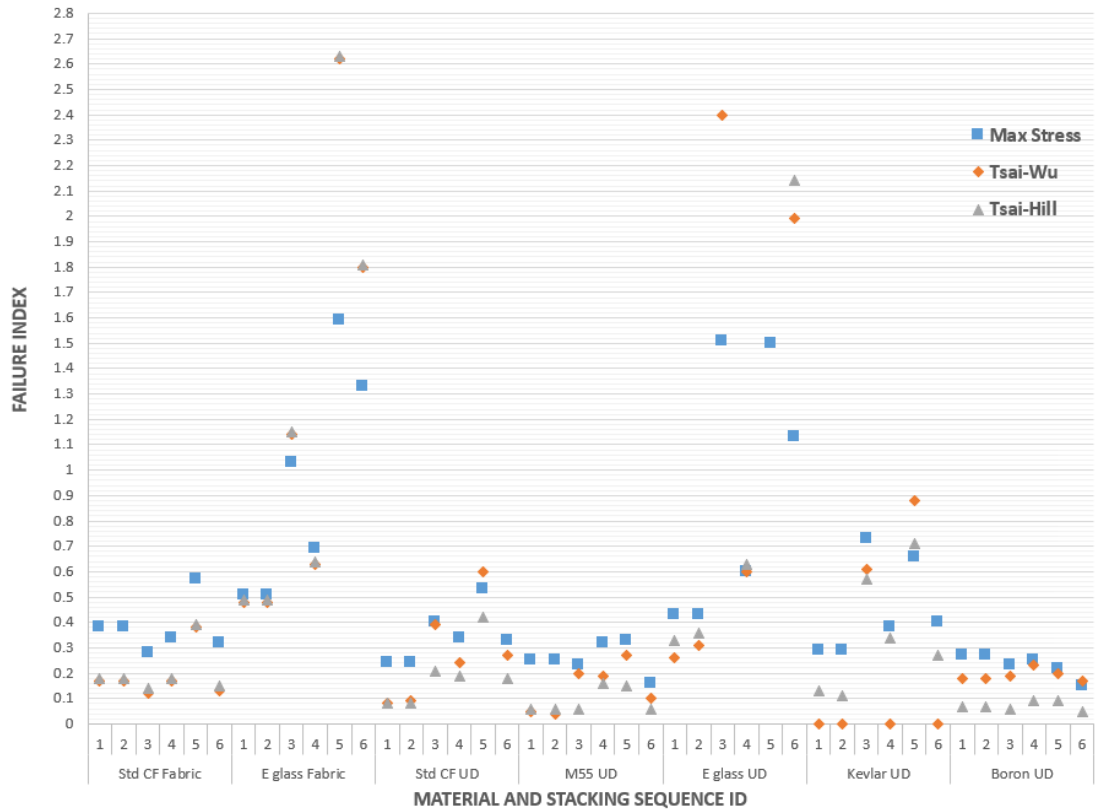


Figure 3.59: Failure index chart with respect to material and stacking sequence.

3.5.2 Conclusion

The analysis revealed critical insights into the failure behaviour of specific materials under certain stacking sequences. For the E-glass fabric, it was found that the stacking sequences 45/-45/0/90, 45/-45/45/-45, and 60/30/-30/-60 led to failure as shown in the Figure 3.60, 3.61, 3.62. This suggests that these particular orientations did not provide adequate balance between the different directional strengths required to handle the applied loads effectively. The inclusion of $\pm 45^\circ$ layers typically aims to improve shear performance, while 0° and 90° layers balance the longitudinal and transverse properties. However, in this case, the combinations were insufficient to prevent failure, likely due to the inherent properties of the E-glass fabric.

Furthermore, the E-glass UD composite failed under the stacking sequences 45/-45/0/90, 45/-45/45/-45, and 60/30/-30/-60 as show in the Figure 3.63, 3.64, 3.65. The consistency of these failures across different forms of E-glass indicates that the inherent material properties or the chosen stacking sequences were not

sufficient to provide the necessary balance of longitudinal, transverse, and shear strengths required for the applied loading conditions.

In conclusion, the failure of these composite materials under specific stacking has been observed and the chosen sequences aimed to optimize performance in particular directions but failed to provide the required multi-directional strength and stiffness. This study highlights the importance of carefully balancing ply orientations to enhance the overall load-bearing capacity and failure resistance of composite laminates. Future work should explore alternative stacking sequences or hybrid composites to achieve a more resilient structural performance, considering their applications.

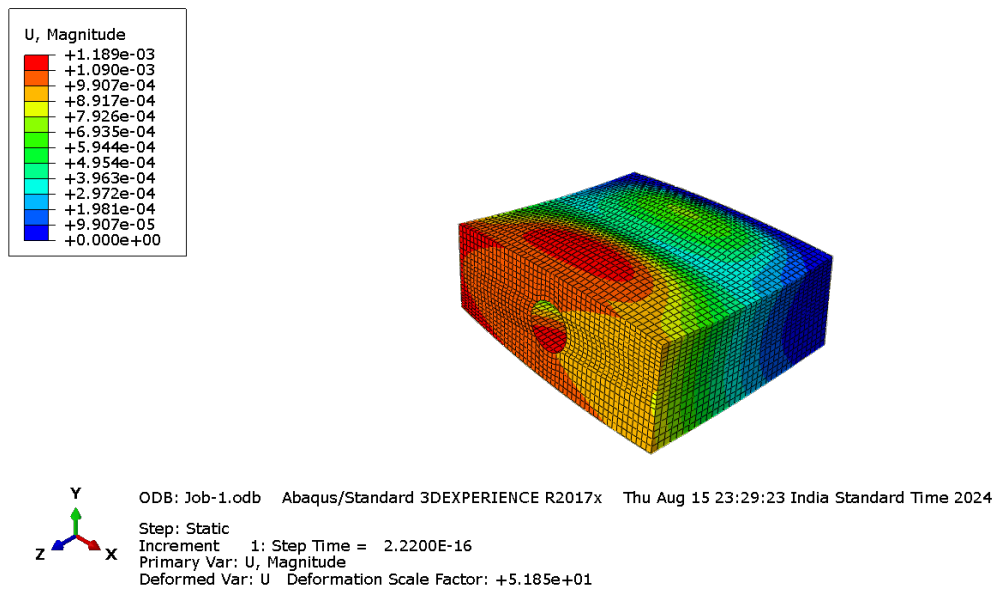


Figure 3.60: E Glass Fabric 45° / - 45° / 0° / 90°.

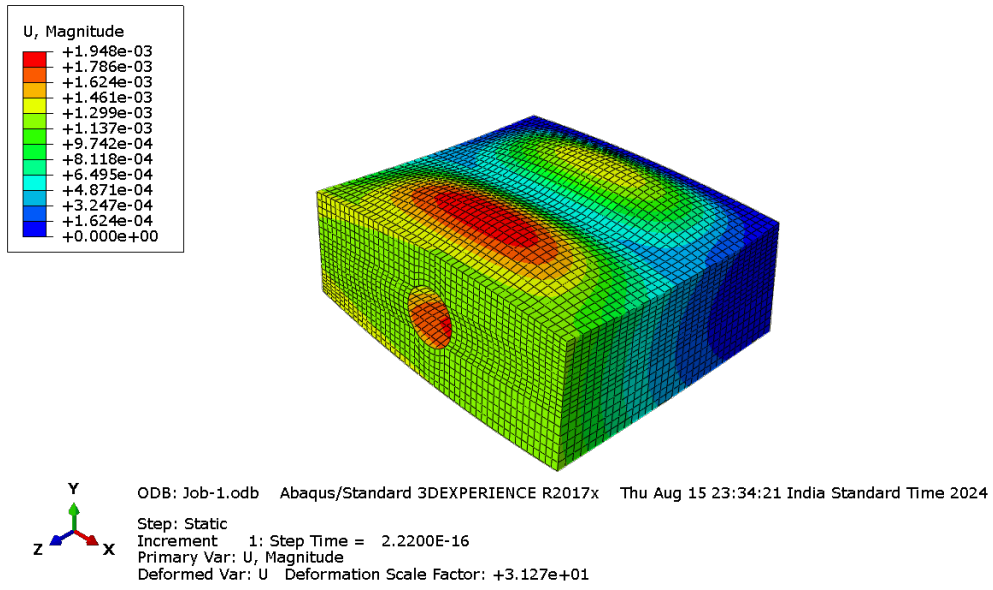


Figure 3.61: E Glass Fabric $45^\circ / -45^\circ / 45^\circ / -4^\circ$.

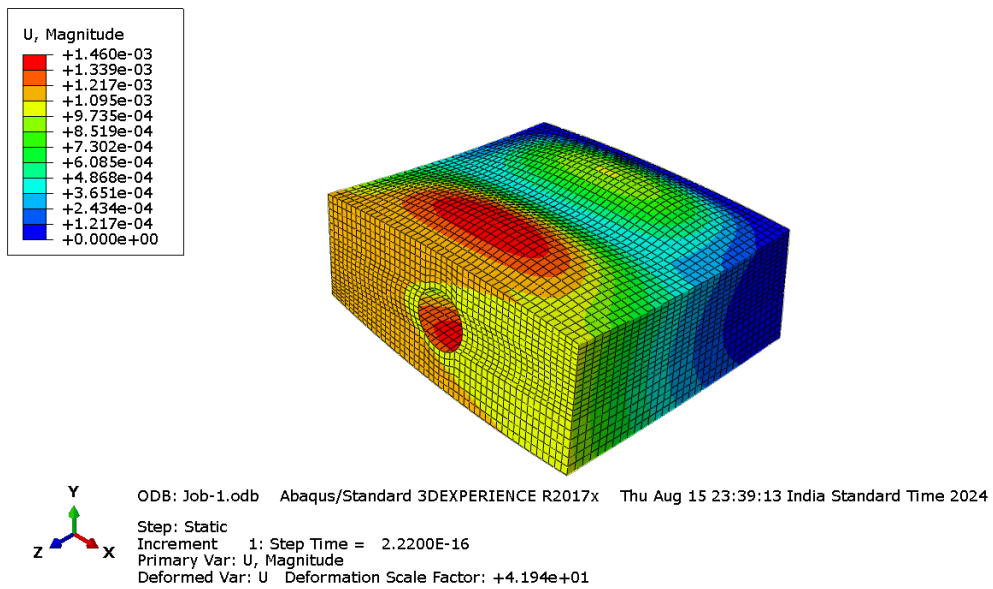


Figure 3.62: E Glass Fabric $60^\circ / 30^\circ / -30^\circ / -60^\circ$.

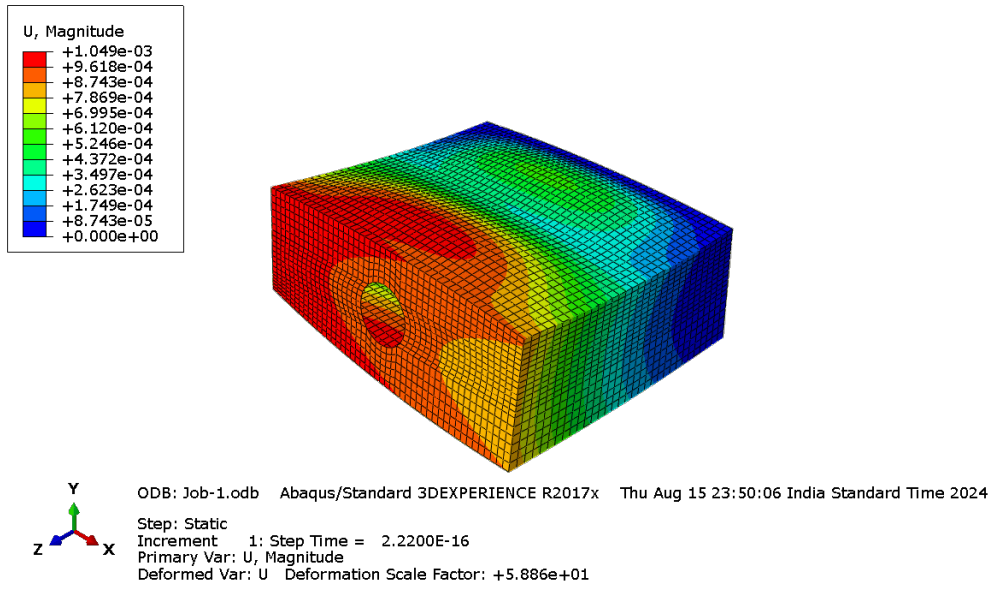


Figure 3.63: E Glass UD $45^\circ / -45^\circ / 0^\circ / 90^\circ$.

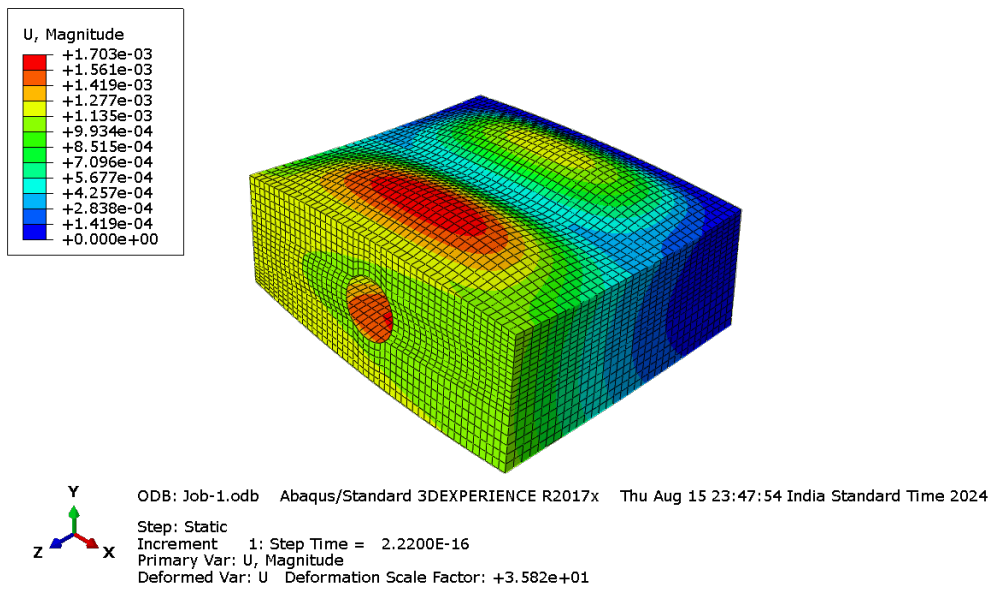


Figure 3.64: E Glass UD $45^\circ / -45^\circ / 45^\circ / -45^\circ$.

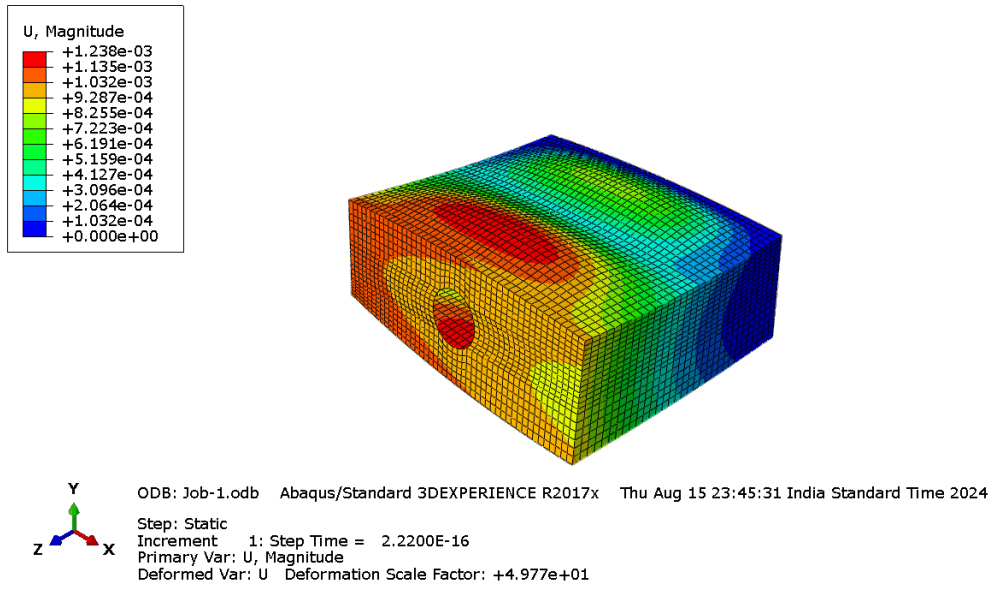


Figure 3.65: E Glass UD $60^\circ/30^\circ - 30^\circ - 60^\circ$.

Chapter 4

Conclusion and Future Perspectives

The thesis concludes that the application of the Carrera Unified Formulation (CUF), in conjunction with Abaqus software, represents a significant advancement in the structural analysis of aerospace components, particularly the central wing box of the Cirrus SR22 aircraft. Through comprehensive analysis, CUF has been demonstrated to offer superior accuracy and computational efficiency compared to traditional Finite Element Methods (FEM). The primary advantage of CUF lies in its ability to simulate the kinematics of a single element with greater detail and precision, leading to more reliable and accurate results. This increased accuracy in representing the behavior of structural elements is critical in the design and optimization of aerospace structures, where precision is paramount.

The study confirms the crucial role of material selection in aerospace engineering, highlighting the benefits of using advanced composites. The use of these materials significantly enhances the performance and efficiency of structural components like the central wing box, enabling weight reduction and improved fuel efficiency without compromising structural integrity. The thesis provides a detailed analysis of the central wing box under various loading conditions, underscoring the importance of optimizing material choices to balance strength, durability, and weight.

Furthermore, the failure analysis conducted using various criteria, including Tsai-Wu and Maximum Stress, has provided valuable insights into the potential failure modes of the central wing box. These insights are essential for developing safer and more reliable aircraft structures. By incorporating failure indices into the analysis, the study identified potential weak points within the structure, allowing for targeted reinforcements and design optimizations.

From a computational perspective, the advantage of CUF is evident in its efficiency regarding both time and cost compared to the classical FEM approach.

The increased accuracy and reduced computational resources make CUF a highly effective method in structural analysis, particularly in the context of complex aerospace structures.

In summary, this thesis highlights the importance of advanced analytical methods like CUF in modern aerospace engineering. The findings contribute to the ongoing development of more efficient, reliable, and high-performance aircraft structures, with significant implications for the aerospace industry. The successful application of CUF and Abaqus in this study paves the way for further research and development, potentially leading to new innovations in aircraft design and safety.

The structural analysis of the Cirrus SR22 wing box using both classical Finite Element Method (FEM) and the Carrera Unified Formulation (CUF) provides a robust foundation for advancing research in several critical areas of aerospace engineering. The findings of this thesis can be expanded upon in the following technical domains:

Exploration of Advanced Composite Materials: The thesis primarily investigates isotropic, Orthotropic and conventional composite materials. Future research could focus on the integration of advanced composite materials, such as hybrid composites, nanocomposites, and smart materials, into the structural analysis framework. These materials exhibit superior mechanical properties, including enhanced specific strength, stiffness, and thermal stability. By incorporating these advanced materials into the CUF and FEM analyses, future studies could optimize the structural performance of the wing box under complex loading scenarios, contributing to the development of lighter and more resilient aerospace structures.

Development of Multi-Scale and Multi-Physics Models: The application of multi-scale modelling techniques within the CUF framework represents a promising avenue for future research. By bridging the gap between micro-scale material behaviour and macro-scale structural response, researchers can achieve a more accurate representation of failure mechanisms, including matrix cracking, fibre-matrix debonding, and delamination. Additionally, extending the analysis to multi-physics domains—such as thermo-mechanical coupling, aeroelasticity, and acoustic-structural interactions—can provide a comprehensive understanding of the wing box's behaviour under diverse operational conditions, paving the way for more robust and multifunctional aircraft components.

Application of CUF to Other Aircraft Components: The methodologies developed in this thesis can be extended to other critical aircraft components, such as the fuselage, empennage, and landing gear. Each component presents unique challenges, including different loading conditions, geometric complexities, and material behaviours. By applying CUF to these components, future studies could achieve a holistic optimization of the entire air-frame, leading to improvements in overall structural integrity, weight reduction, and aerodynamic performance.

Additionally, future research could investigate more complex loading conditions,

such as those encountered during extreme flight maneuvers or in cases of structural damage. This would involve more sophisticated simulations.

In conclusion, the technical contributions of this thesis provide a solid platform for future research in aerospace structural analysis. By building on the methodologies and insights developed here, subsequent studies can drive innovation in aircraft design, leading to more efficient, durable, and high-performance aerospace structures.

Bibliography

- [1] National Transportation Safety Board. *Introduction of Glass Cockpit Avionics into Light Aircraft*. PDF. Archived from the original (PDF) on 5 September 2015. 2015. URL: <https://www.nts.gov/safety/safety-studies/Documents/SR1501.pdf> (visited on 09/11/2015) (cit. on p. 1).
- [2] Aviation Trader. *2010 Beechcraft G36 Bonanza - Piston Single Aircraft*. <https://www.aviationtrader.com.au/listing/for-sale/229968981/2023-cirrus-sr22-g6-turbo-piston-single-aircraft>. Image referenced from the website. Accessed: 20-April-2024. 2024 (cit. on p. 1).
- [3] Wikipedia contributors. *Cirrus SR22*. https://en.wikipedia.org/wiki/Cirrus_SR22. Accessed: 21-April-2024. 2024 (cit. on p. 2).
- [4] Federal Aviation Administration. *TYPE CERTIFICATE DATA SHEET NO. A00009CH Rev. 13*. Technical Report. Archived from the original (PDF) on 19 February 2009. Retrieved 14 October 2008. Federal Aviation Administration, May 2008. URL: https://www.faa.gov/documentLibrary/media/Type_Certificate_Data_Sheet/A00009CH_Rev13.pdf (visited on 10/14/2008) (cit. on p. 2).
- [5] Airspace Aviation LLC. *Do you know the centre wing box of an aircraft?* Accessed: 2024-04-26. 2023. URL: <https://www.linkedin.com/pulse/do-you-know-centre-wing-box-aircraft-airspaceaviation> (cit. on p. 2).
- [6] Abbott Aerospace. *22.16.2. Main Wing Box*. <https://www.abbottaerospace.com/aa-sb-001/22-aircraft-specific-design-features-and-design-methods/22-16-57-wings/22-16-2-main-wing-box/>. Accessed: 2024-10-02. 2024 (cit. on p. 3).
- [7] Immanuvel D., Arulselvan K., Maniiarasan P., and Senthilkumar S. «Stress Analysis and Weight Optimization of a Wing Box Structure Subjected To Flight Loads». In: *The International Journal of Engineering and Science (IJES)* 3.1 (2014). Accessed: 2024-04-27, pp. 33–40. ISSN: 2319-1813. URL: <https://theijes.com/papers/v3-i1/Version-4/E0314033040.pdf> (cit. on p. 3).

- [8] I.D. Erhunmwun and U.B. Ikponmwosa. «Review on Finite Element Method». In: *Journal of Applied Sciences and Environmental Management* 21.5 (2017). Accessed: 2024-04-30, pp. 999–1002. ISSN: 1119-8362. DOI: 10.4314/jasem.v21i5.30. URL: <https://www.ajol.info/index.php/jasem/article/view/161736> (cit. on p. 4).
- [9] Mathijs Peeters, Gilberto Santo, Joris Degroote, and Wim Van Paepegem. «Comparison of Shell and Solid Finite Element Models for the Static Certification Tests of a 43 m Wind Turbine Blade». In: *Energies* 11.6 (2018). ISSN: 1996-1073. DOI: 10.3390/en11061346. URL: <https://www.mdpi.com/1996-1073/11/6/1346> (cit. on p. 4).
- [10] Rakesh Rawat. «Structural Analysis of an Ultra-Light Drift Chamber in Composite Materials for High Energy Particle Physics Experiments». Master’s Thesis. Politecnico di Torino, 2023 (cit. on pp. 5, 21).
- [11] AZoM. *An Overview of Heat-Resistant Superalloys*. <https://www.azom.com/article.aspx?ArticleID=19726>. Accessed: 2024-10-02. 2020 (cit. on p. 5).
- [12] Erasmo Carrera, Gaetano Giunta, and Marco Petrolo. *Beam Structures: Classical and Advanced Theories*. Chichester, UK: John Wiley & Sons, 2011. ISBN: 978-0-470-66552-0 (cit. on p. 6).
- [13] Erasmo Carrera, Francesco Miglioretti, and Marco Petrolo. «Guidelines and Recommendations on the Use of Higher Order Finite Elements for Bending Analysis of Plates». In: *International Journal for Computational Methods in Engineering Science and Mechanics* 12.6 (2011), pp. 303–324. DOI: 10.1080/15502287.2011.627032 (cit. on p. 7).
- [14] Erasmo Carrera, Andreas Büttner, and Paolo Nali. «Mixed Elements for the Analysis of Anisotropic Multilayered Piezoelectric Plates». In: *Journal of Intelligent Material Systems and Structures* 21.7 (2010), pp. 701–717. DOI: 10.1177/1045389X09355525 (cit. on p. 7).
- [15] Northwestern University. *Failure of Composite Materials*. <https://www.mccormick.northwestern.edu/theoretical-applied-mechanics/research/micro-nanomechanics/failure-composite-materials.html>. Accessed: 2024-10-02. 2024 (cit. on p. 8).
- [16] Alberto Racionero Sánchez-Majano. «Multiscale finite element models for the analysis, design and optimisation of variable stiffness composites». PhD thesis. Turin, italy: Politecnica di torino, 2024 (cit. on pp. 10, 16).
- [17] Manish Hassan Nagaraj. «Higher-order layer-wise models for the progressive damage and impact analysis of composite structures». PhD thesis. Turin, Italy: Politecnico di Torino, Jan. 2021 (cit. on p. 10).

- [18] Erasmo Carrera, Marco Cinefra, Marco Petrolo, and Emanuela Zappino. *Finite element analysis of structures through unified formulation*. John Wiley & Sons, 2014 (cit. on p. 10).
- [19] Alfonso Pagani. «Component-wise models for static, dynamic and aeroelastic analyses of metallic and composite aerospace structures». PhD thesis. Politecnico di Torino, 2015 (cit. on pp. 11, 14, 18).
- [20] Rodolfo Azzara. «Nonlinear and Linearized Analysis of Vibrations of Loaded Anisotropic Beam/Plate/Shell Structures». PhD Thesis. Politecnico di Torino, 2023 (cit. on p. 11).
- [21] P.F. Pai. *Highly Flexible Structures: Modeling, Computation, and Experimentation*. Springer, 2007 (cit. on p. 11).
- [22] Riccardo Augello. «Advanced FEs for the micropolar and geometrical nonlinear analyses of composite structures». PhD Thesis. Politecnico di Torino, Jan. 2021 (cit. on p. 12).
- [23] piero chiaia. «advanced finite elements for the large displacement (and large strains) analysis of materials and structures». MA thesis. polytechnic university of bari (cit. on pp. 13, 15, 20).
- [24] J. N. Reddy. *Mechanics of Laminated Composite Plates and Shells: Theory and Analysis*. 2nd. Boca Raton, FL: CRC Press, 2004 (cit. on p. 15).
- [25] E. Carrera and S. Brischetto. «Analysis of Thickness Locking in Classical, Refined, and Mixed Multilayered Plate Theories». In: *Composite Structures* 82.4 (2008), pp. 549–562 (cit. on p. 15).
- [26] Marco Enea. «Global/local and coupled high order FEM-Peridynamics models for fracture analysis of isotropic and composite structures». PhD Thesis. Politecnico di Torino, 2024 (cit. on p. 15).
- [27] M. Narsai; S. Adali; K. Veale; J. Padayachee. «Composite tube testing and failure theory computational comparison». In: *RD Journal* 4.1 (2018), pp. 23–29 (cit. on p. 21).
- [28] PE John J. Engblom Ph.D. *Stress and Failure Analysis of Fiber-Reinforced Composite Structures with Computer-Based Solutions*. Accessed: 2024-08-29. 2020. URL: <https://pdhonline.com/courses/m426/m426content.pdf> (cit. on p. 21).
- [29] R. M. Jones. *Mechanics of Composite Materials*. Accessed: 2024-08-29. Taylor & Francis, 1999. URL: https://sarrami.iut.ac.ir/sites/sarrami.iut.ac.ir/files/files_course/01-mechanics_of_composite_materials_sbookfi.org_.pdf (cit. on p. 21).

- [30] Marianna Maiaru. «Multiscale approaches for the failure analysis of fiber-reinforced composite structures using the 1D CUF». PhD thesis. Politecnico di Torino, 2014 (cit. on p. 22).
- [31] Amedeo Grasso. «Implementation of classical and advanced failure criteria for composite layered structures in FEMAP and assessment of results». MA thesis. Politecnico di Torino, 2018. URL: <https://webthesis.biblio.polito.it/6883/1/tesi.pdf> (cit. on p. 22).
- [32] UAV Navigation. *Flight Envelope*. Accessed: 2024-08-29. n.d. URL: <https://www.uavnavigation.com/support/kb/general/general-system-info/flight-envelope> (cit. on p. 25).